LIFETIMES OF OVERSHOOTING CONVECTIVE EVENTS USING HIGH-FREQUENCY GRIDDED RADAR COMPOSITES

A Thesis

by

DANIEL R. JELLIS

Submitted to the Graduate and Professional School of
Texas A&M University
in partial fulfillment of the requirements for the degree of

MASTER OF SCIENCE

Chair of Committee,	Kenneth P. Bowman
Co-Chair of Committee,	Anita Rapp
Committee Members,	Robert Hetland
Head of Department,	Ramalingam Saravanan

December 2022

Major Subject: Atmospheric Sciences

ABSTRACT

Deep convection that penetrates the tropopause, otherwise known as overshooting convection, is capable of lifting tropospheric air well into the stratosphere. In addition to moisture, these overshoots also transport many chemical species from the boundary layer, affecting the chemistry and radiative equilibrium in the stratosphere. However, it is not currently known how much transport is a result of this mechanism. Therefore, in an attempt to better understand overshooting convection, this study aims to characterize the durations of overshooting events. To achieve this, radar data from Next Generation Weather Radar (NEXRAD) network is composited onto a high-resolution, three-dimensional grid at 5-minute intervals. The resulting product, GridRad, provides echo-top heights that are then compared with tropopause estimates derived from ERA5 reanalysis data. These overshoots are then linked by proximity from one timestep to the next to form tracks. This tracking process is performed for twelve 4-day sample windows in the months May-August of 2017-2019, producing a total of 72,779 tracks. Track characteristics such as duration, mean overshoot area, mean tropopause-relative altitude, and mean column-maximum reflectivity are investigated. Exponential distributions are found for many of these characteristics, with the exception of mean overshoot area, which follows a power-law distribution, and mean column-maximum reflectivity, which has a more complicated distribution. Positive correlations are found between track duration and the remaining track characteristics. A diurnal cycle is observed, with peak track initiation around 16-17 local time. Track-mean duration peaks a few hours earlier, while track-mean area and tropopause-relative height peak a few hours later.

CONTRIBUTORS AND FUNDING SOURCES

Contributors

This work was supported by a thesis committee consisting of Professors Kenneth P. Bowman (co-chair) and Anita Rapp (co-chair) of the Department of Atmospheric Sciences and Professor Robert Hetland of the Department of Oceanography.

Portions of this research were conducted with the advanced computing resources provided by Texas A&M High Performance Research Computing.

All other work conducted for the thesis was completed by the student independently.

Funding Sources

Graduate study was supported by a University Merit Fellowship and Lechner Graduate Grant from Texas A&M University as well as the National Aeronautics and Space Administration Grant 80NSSC19K0341 to Texas AM University.

TABLE OF CONTENTS

Page

LIST OF FIGURES

FIGURE Page

LIST OF TABLES

TABLE Page

1. INTRODUCTION

The transport of material from the troposphere to the stratosphere is dominated by the Brewer-Dobson circulation, characterized by diabatic upwelling in the tropics and downwelling near the poles [2, 3]. This global circulation is the primary mechanism for transport of species with long lifetimes in the troposphere (such as CFCs or CO_2) into the stratosphere. The vertical velocity of this tropical upwelling is very slow, around 0.2 mm/s [4, 5], meaning that shorter-lived species tend to be removed by oxidation and/or wet-deposition processes before reaching the stratosphere. At mid-latitudes, stratosphere-troposphere exchange (STE) occurs mostly as the result of tropopause folding. Through this process, stratospheric air intrudes into lower altitudes and is irreversibly mixed with the troposphere as a result. It has been shown, however, that deep convection is capable of penetrating the tropopause in the mid-latitudes, and that it is a frequent enough occurance to represent a significant stratospheric transport mechanism [6, 1, 7]. Deep convection carries with it tropospheric air, bringing water vapor into the normally very dry stratosphere along with many short- and long-lived species from the boundary layer. It is therefore vital to understand deep convection and the resulting transport of air into the stratosphere, as this water vapor and these trace gas species have an impact on the chemistry and radiative equilibrium of the stratosphere [8, 9, 10, 11, 12, 13].

Deep convection can occur anywhere there is sufficient instability, but is more likely to penetrate into the stratosphere (hereafter overshooting) in areas where the tropopause is lower [1]. Ideal conditions for overshooting are present across North America in the late spring and summer months, with the Great Plains region in the central US being a major hotspot [6]. The summer anticyclone that regularly forms over North America may act to contain the material injected by deep convection in this region, which can prolong the period before the substances are diluted. The resulting mixing and chemistry are not well understood, making this region an attractive target for aircraft campaigns such as the ongoing Dynamics and Chemistry of the Summer Stratosphere (DCOTSS) mission, whose main objective is to sample both fresh and aged outflow from over-

shooting events.

An important part of the DCOTSS mission, and any study investigating deep convection, is the remote detection of overshooting events. Multiple techniques exist for the identification of overshooting cloud tops (OTs). One option is the use of infrared and visible satellite imagery [14, 15, 16], such as from NOAA's Geostationary Operational Environmental Satellites (GOES). Material injection due to an OT often results in an Above Anvil Cirrus Plume (AACP) several kilometers above the anvil [17]. The AACP may be warmer or colder than the surrounding anvil, making automated detection using IR imagery difficult. Visible imagery may be used to detect shadows cast on the anvil by the AACP, however this method depends on the solar zenith angle and is naturally only feasible during the daytime. Another option for the detection of OTs is weather radar. By comparing radar echo heights with a tropopause height analysis, it is possible to identify storms that overshoot the tropopause [6, 1]. This technique avoids the difficulties presented by satellite detection, but introduces a new set of problems stemming from poor radar coverage and coarse vertical resolution.

While we know when and where overshooting convection tends to occur, there is still much that is not well understood. Some topics of interest include how much material is transported to the stratosphere, how long injected material remains, the impact of overshooting on stratospheric chemistry, what environmental conditions are favorable for overshooting, and how climate change will affect the frequency of overshoots in the future. As a step toward understanding the processes that transport material from the troposphere to the stratosphere through deep convection, this research aims to characterize the lifetimes of overshooting events using observations. This is achieved through the use of overshooting storm analyses from the Next Generation Weather Radar (NEXRAD) network. Radar analyses are conducted across the continental United States at 5-minute intervals, which is approximately the time required for a NEXRAD radar to complete a volume scan when observing convection. For this study a total of twelve 5-day analysis periods are used, covering the middle of each summer month (May - August) for the years 2017-2019. Overshooting events are identified for each analysis time. Storms identified in sequential analyses

are then linked together based on proximity to form tracks. This provides a multi-year sample of overshooting tracks across the warm-season months, which allows estimation of the statistics of overshooting-event durations and other properties.

2. DATA

2.1 NEXRAD

NEXRAD comprises 160 WSR-88D high resolution S-band Doppler radars worldwide, 143 of which provide nearly complete coverage over the contiguous United States, as shown in Figure 2.1 [18]. These radars measure reflectivity, mean radial velocity, and velocity spectrum width by pulsing a 0.95° wide conical beam while sweeping a full 360° of azimuth at multiple elevation angles. The number of elevation angles and scan time varies based on the volume coverage pattern (VCP) chosen by the radar operator. When convection is nearby, the radar will normally sweep through 14-15 elevation angles between 0.5° and 19.5° over the course of 4-6 minutes.

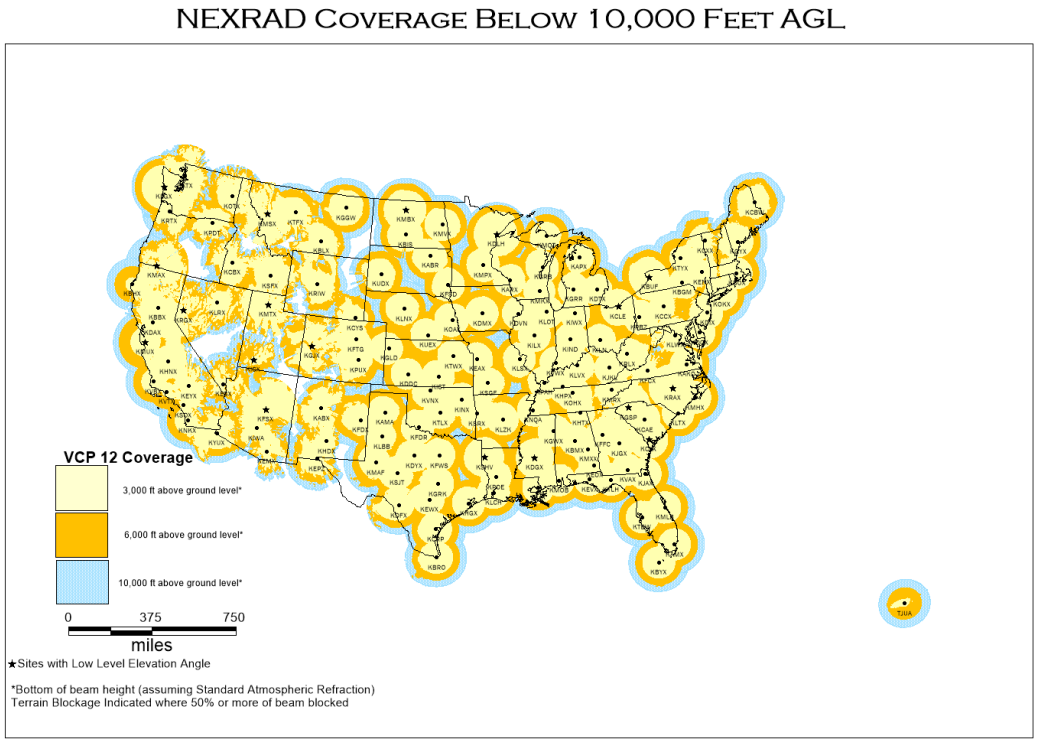

Figure 2.1: NEXRAD Radar Coverage below 10,000 ft. This image was retrieved from the NWS Radar Operations Center website, https://www.roc.noaa.gov.

WSR-88D radars are capable of detecting reflectivity signals as low as -42 dBZ at a range of 1 km, increasing to approximately 11 dBZ at the maximum range of 460 km. For the analysis times used in this study the data is provided at 'super-resolution', meaning for the lowest 3-5 elevation angles the azimuthal resolution is 0.5° and the range resolution is 250 m, while at higher elevation angles the azimuthal resolution is 1° , and the range resolution is 1 km. The complete volume scans for each radar (Level-II data) are downloaded from Amazon Web Services (AWS) for this project.

2.2 ERA5

Meteorological parameters, such as temperature and pressure, are taken from the ERA5 Reanalysis, which is produced by the European Centre for Medium-Range Weather Forecasts (ECMWF). For this study we use ERA5 hourly analyses on a $0.75^\circ \times 0.75^\circ$ global grid with 37 standard pressure levels from 1000 mb to 1 mb. ERA5 covers the period from 1950 to present day [19].

3. METHODS

3.1 GridRad Compositing

Multiple previous studies have been conducted on the effectiveness of compositing 3-D radar data [20, 21, 22]. In this research, Level 2 NEXRAD data are composited onto a three-dimensional longitude-latitude-altitude grid using techniques described in Solomon et al. (2016). During the compositing process, each radar observation is first converted from polar coordinates to a regular rectangular grid. To more accurately portray the vertical structure of the observed storms, a single radar beam may only contribute reflectivity to gridboxes within 0.75 km above and below the center of the beam, which corresponds to a vertical width of 2-4 gridboxes. In cases where multiple observations contribute to a single grid volume, a Gaussian weighting scheme is used in both space and time. Observations that are nearer to the radar and closer to the analysis time are weighted more heavily than more distant observations. To ensure all available data are included, all volume scans within ± 10 minutes of the analysis time are checked for azimuthal sweeps that occur within ± 5 minutes of the nominal analysis time. The resulting Gridded Radar product (GridRad) has a horizontal resolution of 48 bins per degree longitude or latitude ($\sim 0.02083^\circ \times 0.02083^\circ$) and a vertical resolution of 0.5 km from 0-7 km, and 1 km above 7 km and up to 22 km [23].

In order to investigate the development and lifetimes of overshooting tops, a high analysis frequency is required. The Brunt-Väisälä period in the lower stratosphere is typically 10-12 minutes, meaning we require sampling intervals of no longer than 5-6 minutes to capture gravity-wave oscillations. As discussed above, NEXRAD radars take about 5 minutes to complete a volume scan. This means a 5-minute interval is both the shortest meaningful interval due to operational constraints, and the longest acceptable interval when considering the characteristic timescale. Consequently, radar analyses are computed at regular 5-minute intervals for this study. To sample diurnal and seasonal variations and to reduce sampling errors due to interannual variability, 5-day periods at the center of each month from May-August (the 13th-17th) are analyzed for the years

2017-2019.

3.2 Echo-Top Identification

To identify echo tops above the tropopause, the tropopause altitude is computed from the ERA5 reanalysis data. First, temperature values in each column of the ERA5 grid are linearly interpolated onto a regular 250 m altitude grid. Then, the World Meteorological Organization (WMO) definition of the tropopause is applied. The WMO defines the tropopause to be the lowest level where the absolute value of the lapse rate falls below 2 K/km and the mean lapse rate of the 2 km layer above (and including) this level does not exceed 2 K/km. In the vicinity of tropopause folding, multiple levels may meet these criteria. In these cases, the lower or 'primary' tropopause is used. For validation of the quality of tropopause altitudes derived from gridded reanalyses, see e.g. Reichler et al. (2003) [24], Solomon et al. (2016) [6], and Tegtmeier et al. (2020) [25].

Once the radar compositing is complete, echo-top surfaces are generated for various reflectivity thresholds. These surfaces provide echo-top heights for comparison with the ERA5 tropopause, making identification of OTs possible. For this study 10 dBZ is chosen as the threshold, as it is low enough to capture most meteorological echo and high enough for reliable detection. The echo-top altitude, if it exists, is the altitude of the highest valid radar echo in each grid column such that the reflectivity exceeds the threshold, there are two valid measurements in the grid boxes directly below that altitude, and the column-maximum reflectivity is at least 30 dBZ. These criteria help to eliminate radar artifacts such as sun and hail spikes, which are often very narrow and not situated over a convective core.

3.3 Overshoot Tracking

The GridRad echo-top heights are compared to the height of the tropopause from the ERA5 data (Z_{rel} = Z_{echo} - $Z_{tropopause}$), and all grid boxes with Z_{rel} above a specified threshold, chosen here to be 1 km, are identified as overshooting. Sensitivity testing for this threshold and other tracking parameters is discussed in appendix A. Adjacent overshooting grid boxes (including diagonally-adjacent boxes) are grouped to form overshooting regions. The grid box with the highest Z_{rel}

within each region is considered to be the overshoot location. Small regions may be ignored in tracking through the use of a minimum region-size threshold. For this analysis, it is required that a region consist of at least four grid boxes containing echo tops at least 1 km above the tropopause. This is done to minimize insignificant and transient radar echoes. Due to the fact that a single gridbox varies in size across the sample region depending on latitude, from a minimum of 3.45 km^2 at the northern edge to a maximum of 4.8 km^2 to the south, the minimum region-size threshold corresponds to a minimum overshoot area of 13.8 km^2.

Overshoot-region analyses are carried out for each analysis time. Two regions in sequential analyses are matched by the tracking algorithm if they are separated by less than a specified distance threshold, chosen here to be 7 km. This constrains the horizontal speed of the region to be less than 84 km/h over the 5-minute interval. If multiple regions at the second analysis time lie within the distance threshold, the closest region is selected. This process is repeated with subsequent analysis times until no region is found within the distance threshold. A sequence of linked regions (or a single, unlinked region) is referred to here as a track. Any new regions that are not matched are considered to be the potential start of a new track. Figure 3.1 shows an example of this process. Two regions are identified for timestep 1 (left), and three for timestep 2 (right). Within a search radius (shown in orange), distances between old and new regions are computed and the nearest regions are linked. As a result, region 2a will be linked with region 1a, region 2c will be linked with region 1b, and region 2b will be the start of a new track. Tracking is performed for an entire 5-day period, and repeated for each of the 12 separate periods.

3.4 Sampling

The tracking technique is applied to the sequence of 5-minute analyses within each 5-day analysis period. To avoid underestimating the lengths of overshoot events that extend beyond the beginning or end of the 5-day analysis period, a 4-day sampling window is selected from within each 5-day period. The sampling window begins and ends at 1600 UTC, which is approximately the minimum in the diurnal precipitation cycle for the study region (see Fig. 4.3). All tracks that begin within this period are included in the analysis, including those that extend beyond the end

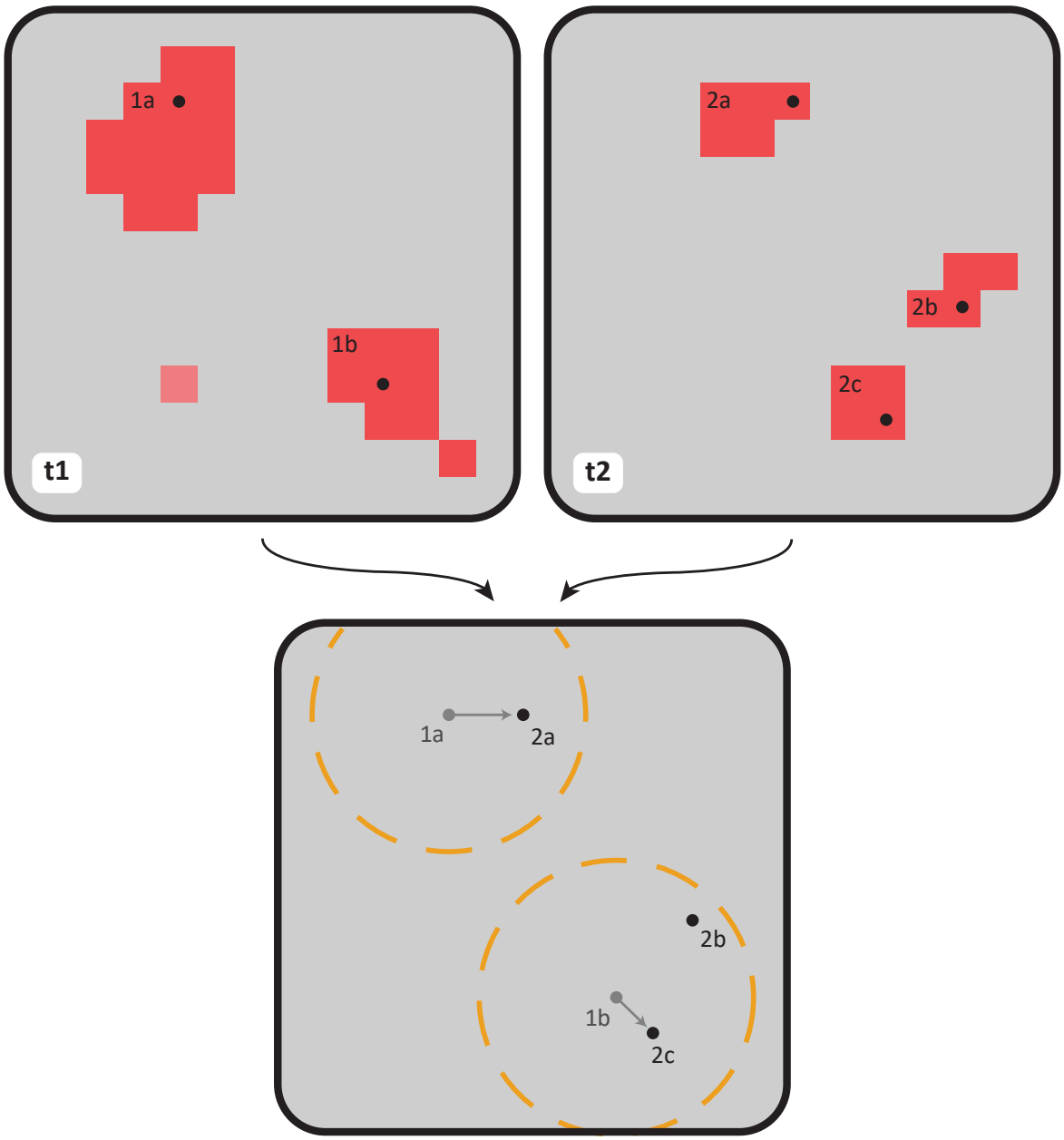

Figure 3.1: Diagram of OT tracking procedure. The top panels show identified overshooting regions (red) and locations of peak Z_{rel} for each valid region. The bottom panel shows the matching of OTs between timesteps.

of the sample period. This approach avoids biasing the diurnal sampling and provides an 8-hour buffer between the end of the sample window and the end of the radar data. Considering no tracks are observed with a duration longer than 2 hours (see Figure 4.6), the full duration of all sampled tracks is observed. The sample for this study thus contains 48 days of 5-minute analyses, for a total of 13,824 analyses.

3.5 Difficulties

The limitations of radar sampling present some challenges in the overshoot-region identification process. As discussed in the Data section, the radar scan frequency limits the temporal resolution to 5 minutes, while the spatial resolution of the radar limits the GridRad resolution to approximately a 2 km horizontal grid with 1 km vertical spacing. The lack of scan angles at higher elevations is also a factor, as individual radar sweeps are often visible as bands on the echo-top fields. Overshooting regions that are moving radially away from or toward a radar will pass through these bands and the dead zones between them, and will be split into multiple tracks as a result.

Additionally, large sections of anvil may appear to be above the tropopause, when most likely only small portions actually penetrate into the stratosphere. This may be due to the fact that the ERA5 model, as a hydrostatic model, cannot explicitly represent convection. Thus, in areas where the tropopause has been raised due to convective influence, the ERA5 tropopause may underestimate the actual height of the tropopause. These situations generate long-lived tracks with large areas in cases where the whole anvil is above the 1 km threshold for several timesteps. If the anvil is very close to the threshold for an extended period, many small, short-lived tracks are formed as regions appear and disappear from one timestep to the next. This is one of the issues that the 30 dBZ column-maximum reflectivity threshold aims to mitigate, as these regions are often displaced from the convective core. However, it does not entirely resolve the issue, and it is difficult to claim that these regions should be thrown out entirely. As such, they are included with the qualification that the number of shorter-lived overshoots, as well as the area of many overshoots are overestimated in this study.

4. RESULTS

4.1 Overview

A total of 183,131 overshooting regions are identified from the high-frequency radar analyses, which corresponds to an average of about 10 regions per analysis or 3,000 regions per day. The locations of all regions and the region count by hour are shown in Figures 4.1 and 4.3, respectively. These results can be compared to Figures 7 and 9 from Cooney et al. (2018) [1], provided here as Figures 4.2 and 4.4. The sample period used in Cooney et al. is much larger, covering March-August at hourly intervals across a 10-year period from 2004-2014. The criteria used to identify overshooting regions are similar to those used in this study (minimum of 1 km above the tropopause, two valid echo below the echo top), only without the 30 dBZ column-maximum reflectivity requirement. One would expect the introduction of this threshold to reduce the number of regions observed, however both studies identify about 10 regions per analysis. This may be due to the inclusion of March and April in the sample period of Cooney et al., as there tend to be fewer overshoots during these months. The diurnal patterns also match up remarkably well, with very similar shape and peak overshoot detection at 23-00Z. The geographic distributions are roughly similar; both identify the large maximum over the central plains, as well as a secondary maximum in the southeast US. The agreement of the results presented in this study with the climatology of Cooney et al. provides support for the claim that the relatively small 4-day sample windows used here are representative of the greater set of overshoots.

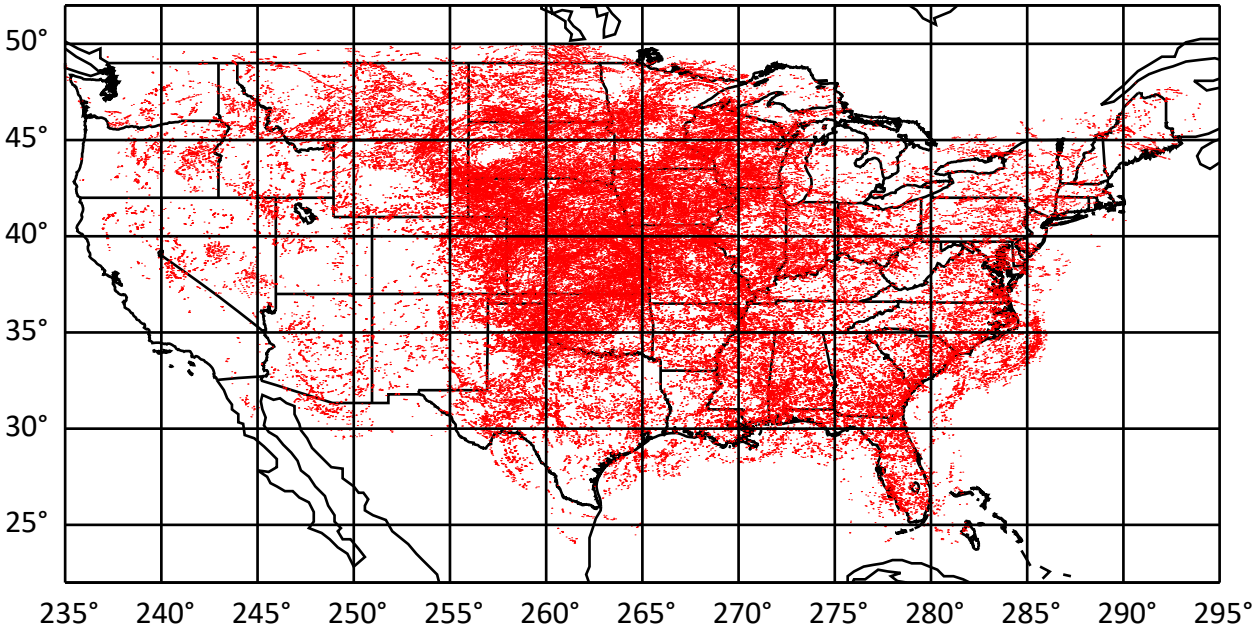

Figure 4.1: Geographic distribution of overshooting regions. Random noise has been added to reduce overlapping of points.

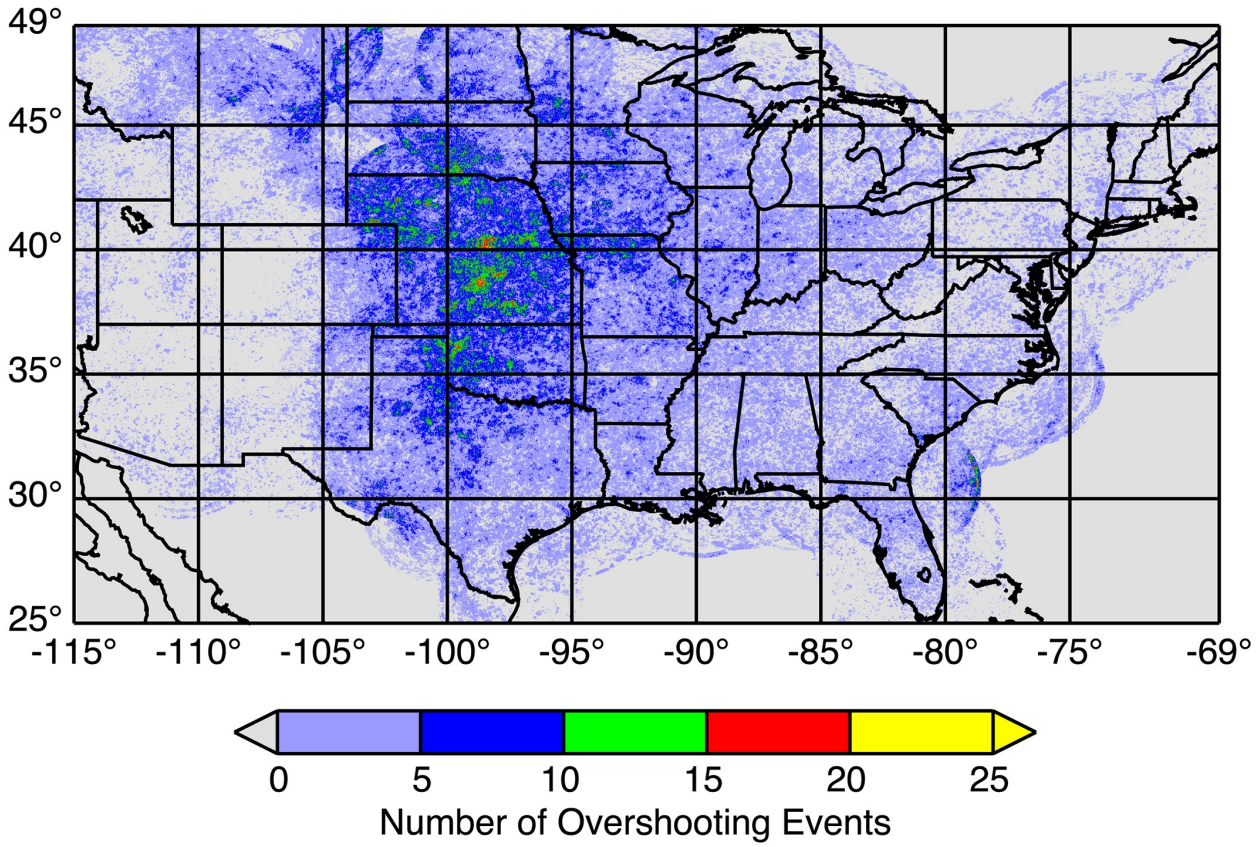

Figure 4.2: Geographic distribution of hourly overshoot regions. Reprinted with permission from Cooney et al. (2018). [1]

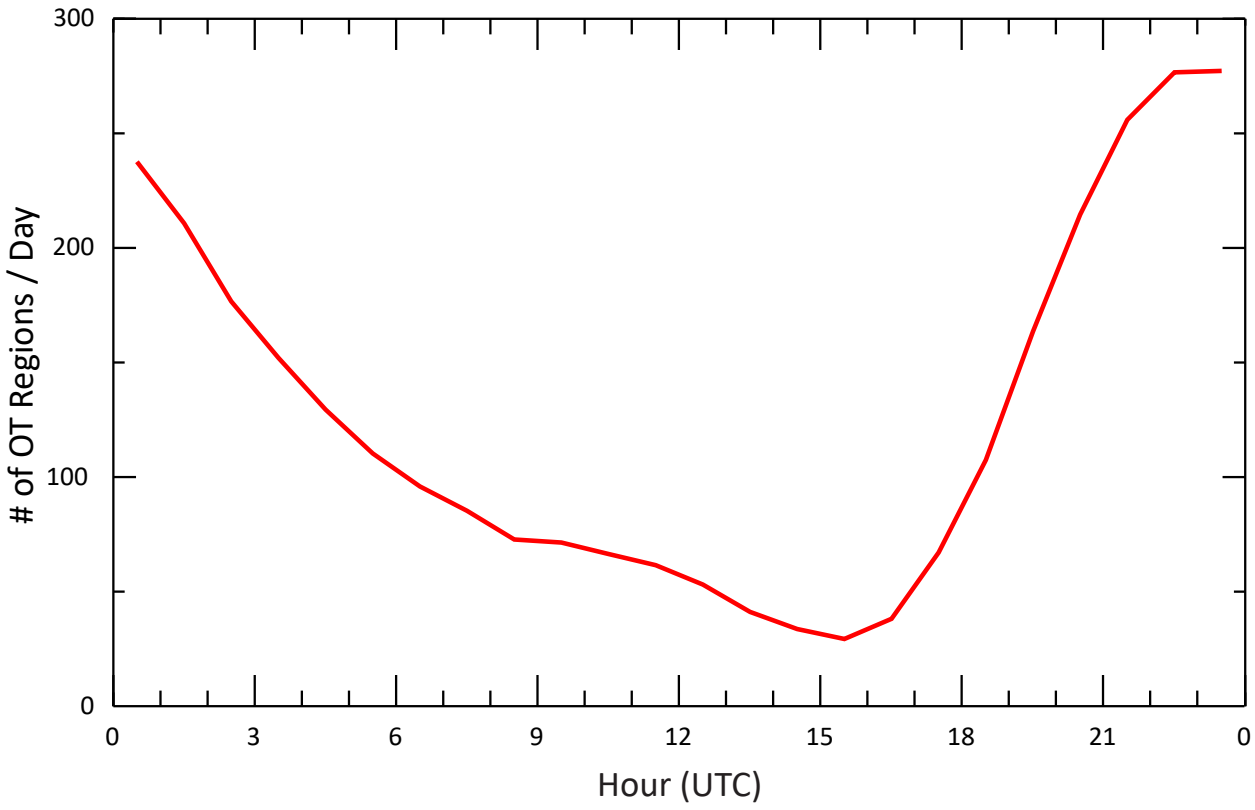

Figure 4.3: Diurnal cycle of overshooting-region count. Values are provided in average overshoots per day for each hourly interval.

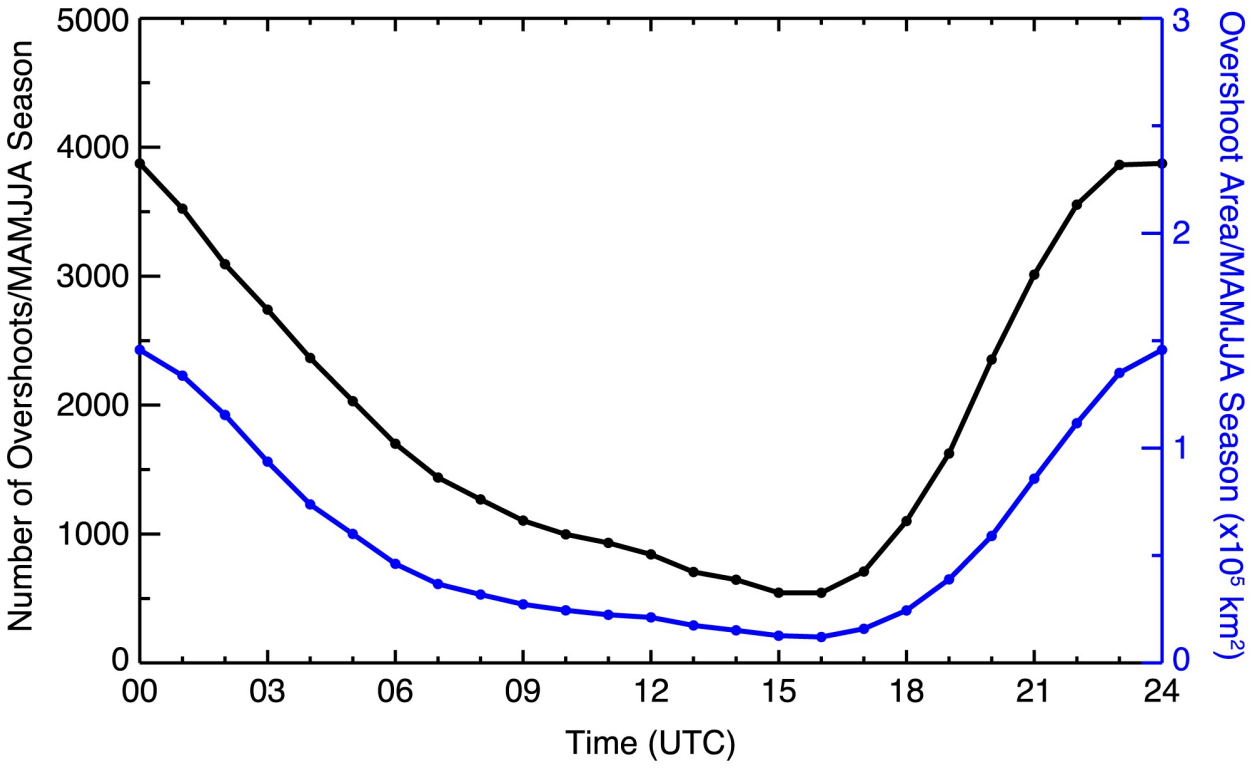

Figure 4.4: Diurnal cycle of hourly overshooting region count and area. Reprinted with permission from Cooney et al. (2018). [1]

From these regions, the tracking algorithm forms a total of 89,000 tracks (including single-timestep tracks) of which 72,779 are selected by the sample windows. This corresponds to 81.8% (about 4/5) of the total tracks, as is to be expected when sampling a 4-day window from a 5-day period. The chosen sample periods represent 16 out of the 123 days in May-August, with an average of 1,516 tracks per day. Scaling these results, we can estimate that there are 186,496 tracks per year in the months May-August, or 46,624 per month on average. Note that individual thunderstorms may have multiple or cyclic updrafts, with overshooting tops that repeatedly form and dissipate. It is therefore important to make the distinction between overshooting storms and overshoot tracks, as a single storm may give rise to dozens of tracks.

The mean tracks per day for each sample period are shown in Table 4.1. Values vary by a factor of nearly 3 between the minimum in July 2017 and the maximum in June 2019. This is due to a combination of the seasonal cycle of overshooting, interannual variability, and sampling error. This table also provides the mean values for each month and year. As this sample includes 12 total days within each month, we are able to calculate the standard error of the mean tracks per day for each month. This is achieved by applying the formula $SE = \frac{\sigma}{\sqrt{n-1}}$ where SE is the standard error, σ is the standard deviation of the sample, and n is the number of items in the sample, in this case 12 days. It is worth noting that nearly twice as many tracks used in this analysis occurred in June as in July. The geographic distribution of sampled tracks is shown in Figure 4.5. The majority of tracks initiate over the central Great Plains region, with a smaller maximum over the southeastern US.

	May	June	July	August	Total
2017	1821	1961	809	1349	1485
2018	1655	1892	1141	1191	1470
2019	891	2343	1285	1858	1594
Total	1456 ± 334	2065 ± 156	1078 ± 110	1466 ± 158	1516

Table 4.1: Number of overshooting tracks per day for each of the twelve sample periods, along with monthly and yearly means.

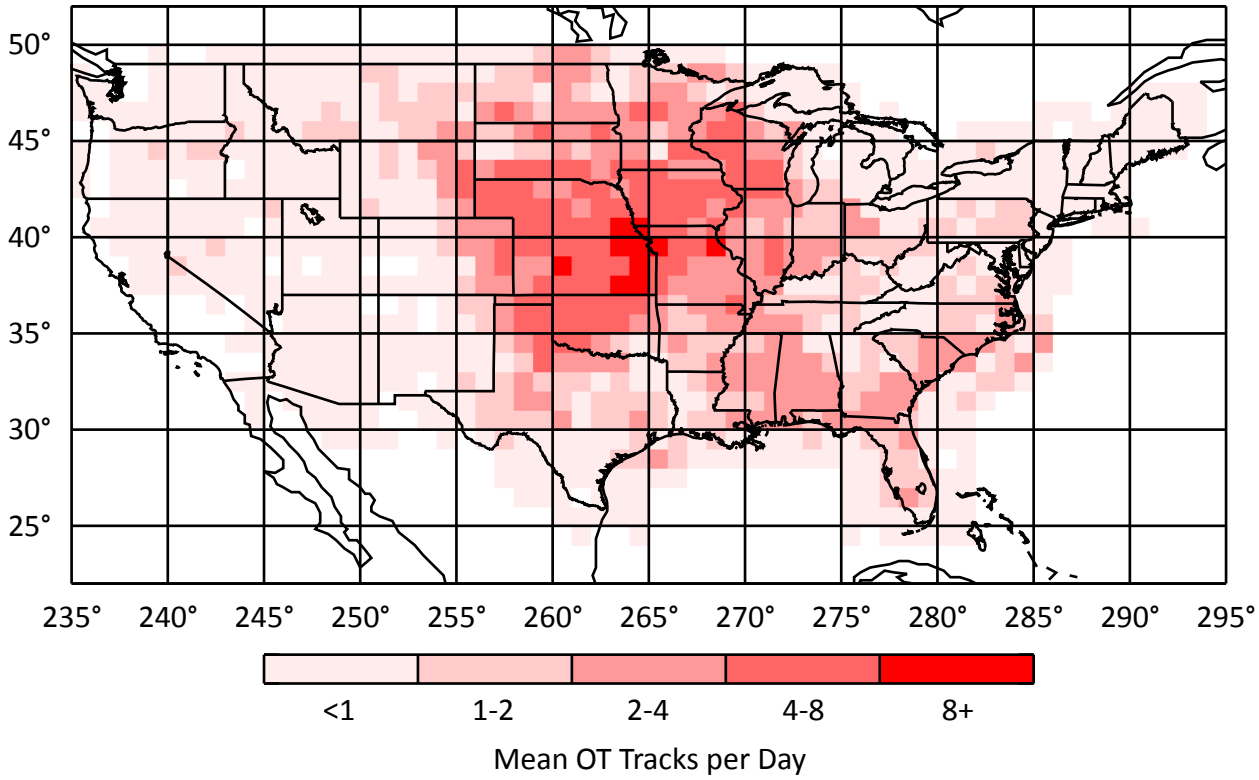

Figure 4.5: Mean number of overshoot tracks that initiate in each bin daily. Bins are $1^\circ \times 1^\circ$.

4.2 Overshoot Duration

Due to the sampling frequency, the precision of track lengths are 5 minutes and durations are integer multiples of 5 minutes. The histogram of these durations is shown in Figure 4.6, along with the cumulative distribution function (CDF) and exponential fit. About half of all tracks (49.4%) have a duration of 5 minutes, and the mean duration is 10.27 minutes, or just over two analysis timesteps. The maximum duration observed is 125 minutes. An exponential fit is applied by performing linear regression on the natural logarithm of the track count vs the track duration. Only bins with at least one track per day are considered, which corresponds to track durations of up to 60 minutes. The resulting slope shows that: $n \propto e^{\frac{t}{\hat{t}}}$, where n is number of tracks, t is track duration in minutes, and $\hat{t}$ is the e-folding timescale with a value of 8.13 minutes. The Brunt-Väisälä period in the lower stratosphere is typically 10-12 minutes, which will serve as the characteristic timescale for overshooting events. There are 18,598 tracks (25.6%) observed with durations of 15 minutes or longer, so while the majority of tracks persist for one or fewer Brunt-Väisälä periods there are many that persist for much longer.

The geographic distribution of track duration is shown in Figure 4.7. Tracks that initiate over the central plains have, on average, a shorter duration than those that initiate elsewhere. Most notably, there is a maximum in mean duration across the southeast, with several bins in Alabama, Georgia, South Carolina, and Florida having a mean duration of over 12.5 minutes.

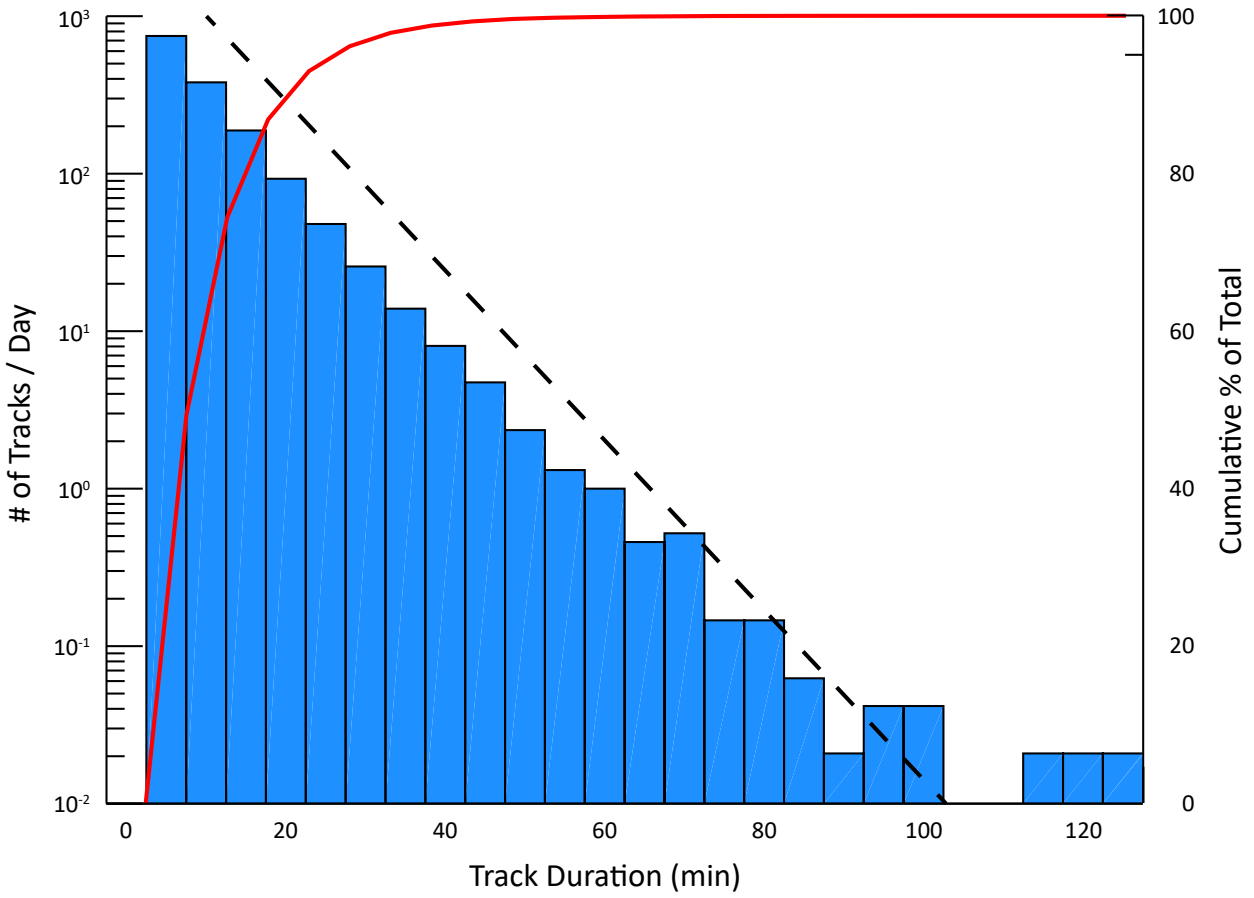

Figure 4.6: Pooled histogram of overshoot-track durations for all sample periods. The cumulative distribution is shown in red. The dashed line represents an exponential fit with an e-folding time of about 8 minutes.

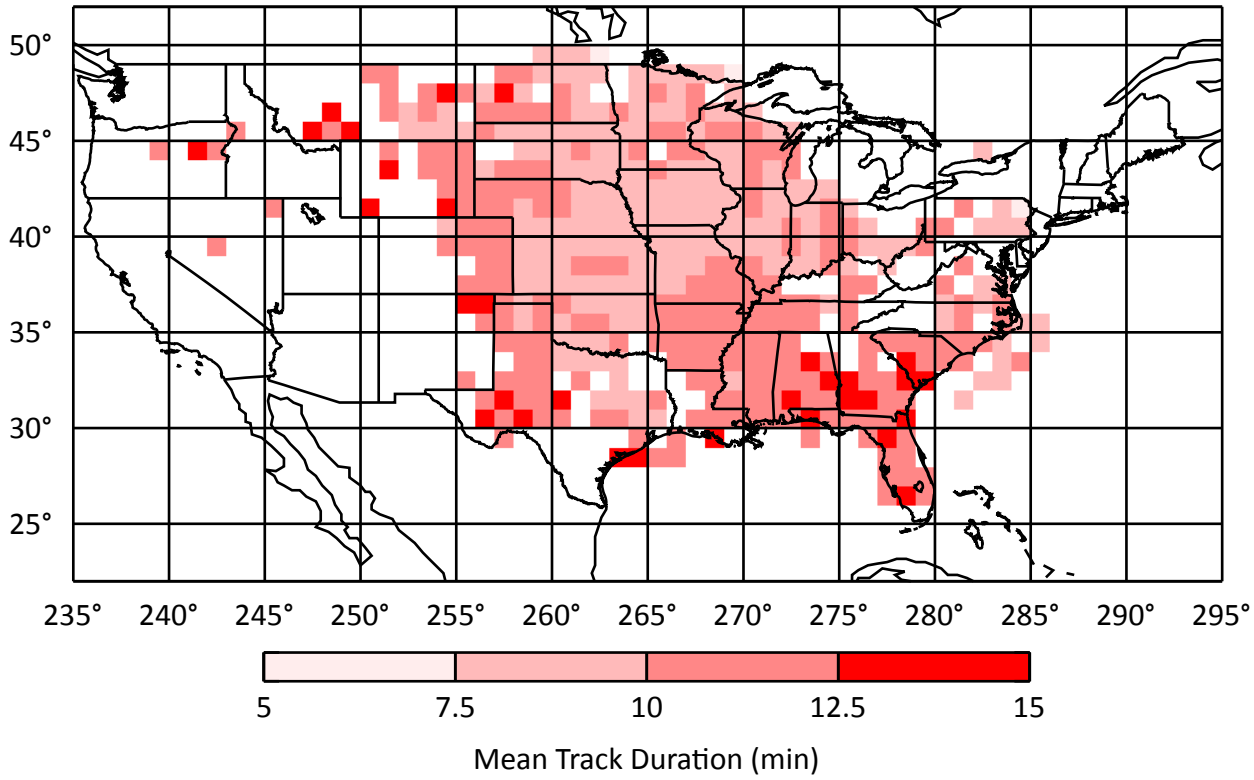

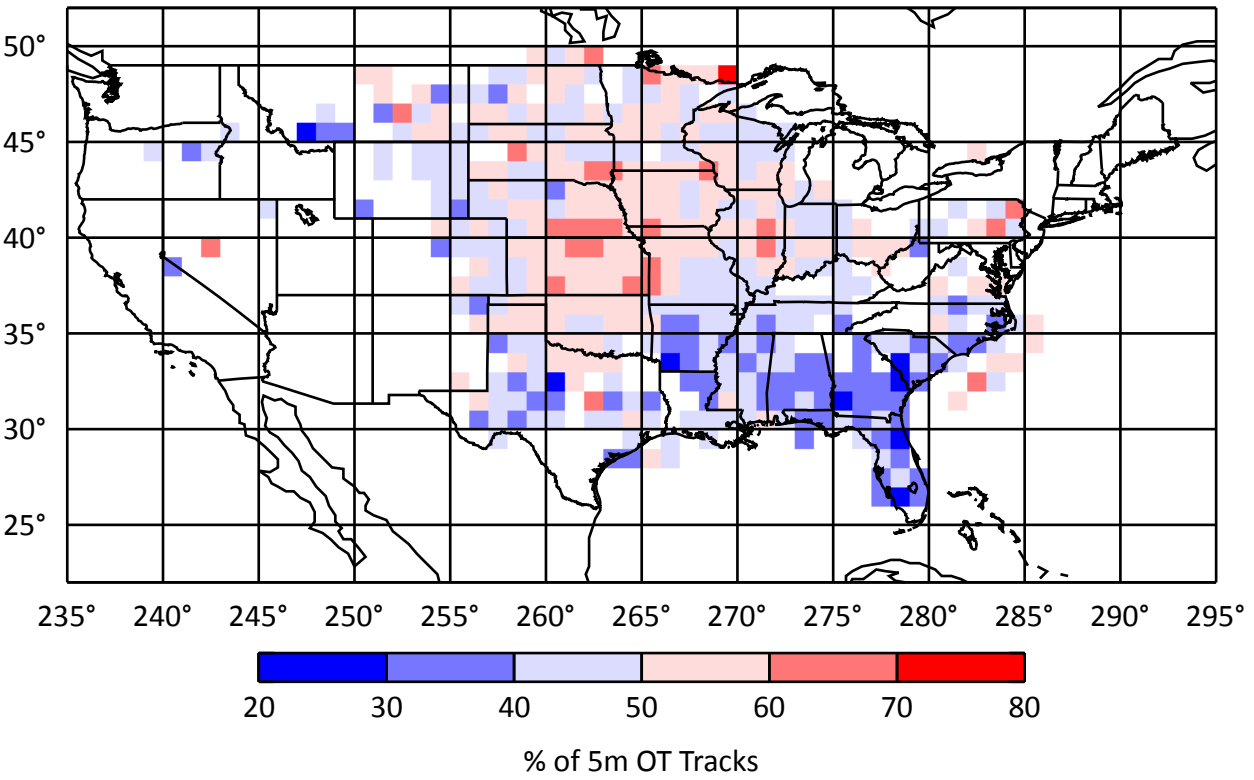

Figure 4.7: Geographic distribution of track duration. Mean values are shown for each 1° by 1° bin. Only bins with at least one track per day are shown.

4.3 Tropopause-Relative Echo-Top Height

The track-mean tropopause-relative echo-top height is used to characterize the Z_{rel} of a track. There is a minimum Z_{rel} threshold of 1 km applied during tracking, so it is impossible for a track to have a lesser value. The histogram and CDF of Z_{rel} are shown in Figure 4.8, along with an exponential fit. Approximately 50%, 80%, and 95% of tracks have a maximum Z_{rel} of less than 2, 3, and 4 km respectively. The fit is applied to the histogram by performing linear regression on the natural logarithm of the track count vs the track-mean Z_{rel}. The resulting slope shows that: $n \propto e^{\frac{z}{\hat{z}}}$, where n is number of tracks, z is the track-mean Z_{rel} in km, and $\hat{z}$ is the e-folding height with a value of 0.77 km. This histogram is consistent with the instantaneous (as opposed to track-mean) Z_{rel} histogram presented in Figure 12 of Cooney et al. (2018) [1], provided here as Figure 4.9.

The geographic distribution of track-mean Z_{rel} is shown in Figure 4.10. There is an area of high track Z_{rel} in the central plains covering most of Kansas, with bin-average values between 2.5 and 3 km above the tropopause. This coincides with the maximum of track count shown in Figure 4.5 as well as the minimum in track duration from Figure 4.7. There is a positive correlation between track-mean Z_{rel} and duration, shown in Figure 4.11. To generate this figure, track-mean Z_{rel} values are first binned by track duration, and the mean of each bin is then found. A linear regression is applied to the plot, resulting in a fit with slope of 86.5 minutes/km. This result makes intuitive sense, with overshoots that penetrate further into the stratosphere tending to persist for longer. However, the geographic distributions seem to contradict this conclusion, considering several bins in the central plains have high mean Z_{rel} and low mean duration. Manual inspection reveals that many tracks in this region appear to be from storm anvils, and as discussed in the methods section this gives rise to a large number of 5-minute tracks. Indeed, around 60% of the tracks in these bins have durations of 5 minutes, well above the value of 50% found for all tracks.

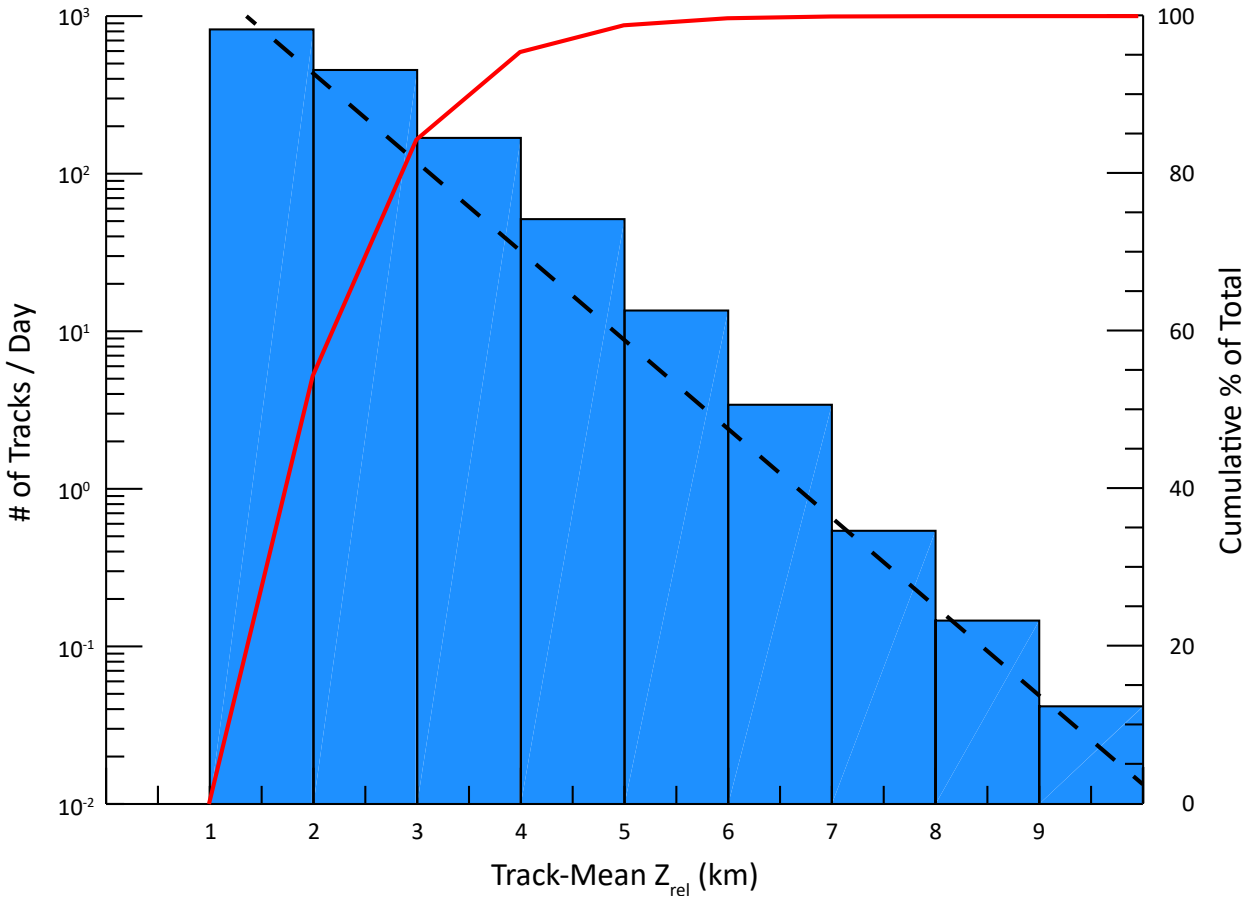

Figure 4.8: Pooled Histogram of track-mean tropopause-relative echo-top height for all sample periods. The cumulative distribution is shown in red. The dashed line represents an exponential fit with e-folding height of about 0.77 km.

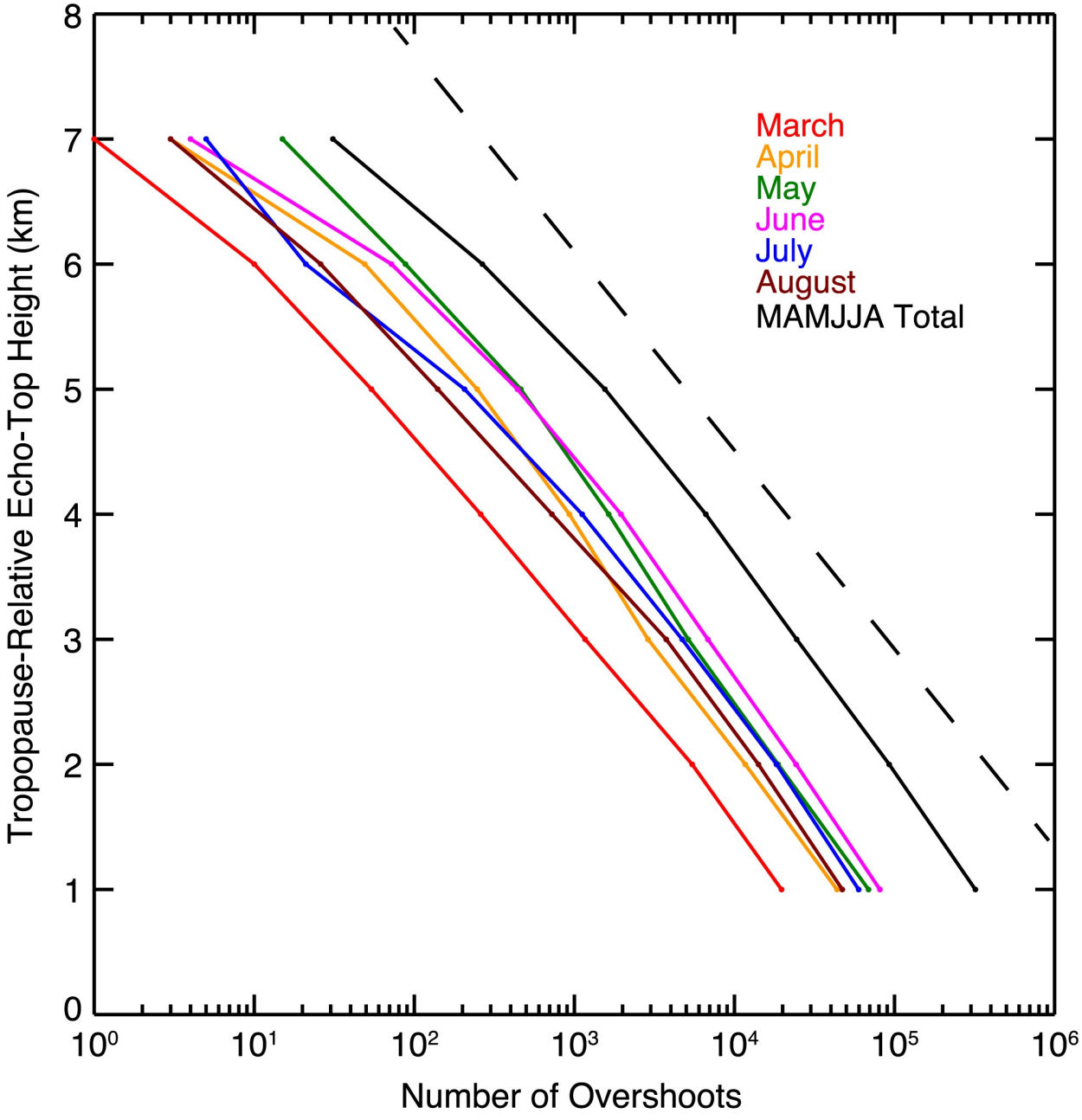

Figure 4.9: Histogram of hourly region Z_{rel}. Reprinted with permission from Cooney et al. (2018). [1]

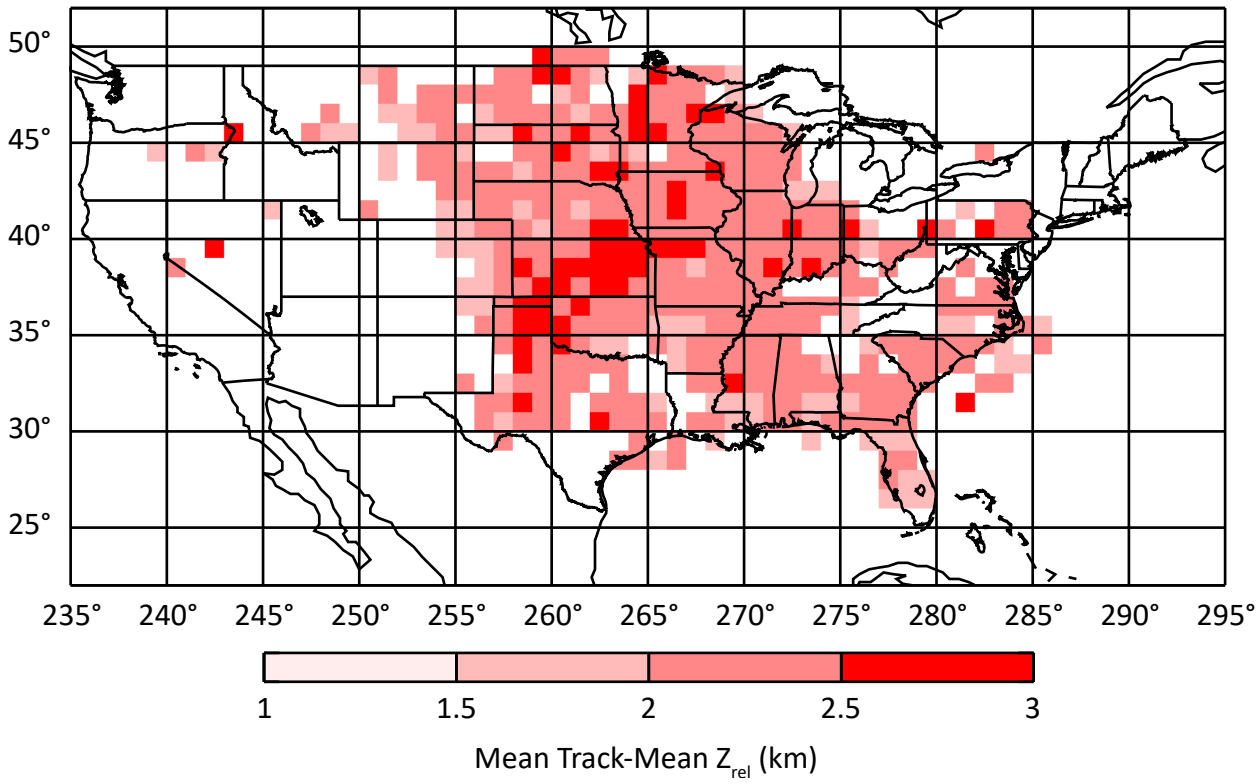

Figure 4.10: Geographic distribution of track-mean tropopause-relative echo-top height. Mean values are shown for each 1° by 1° bin. Only bins with at least one track per day are shown.

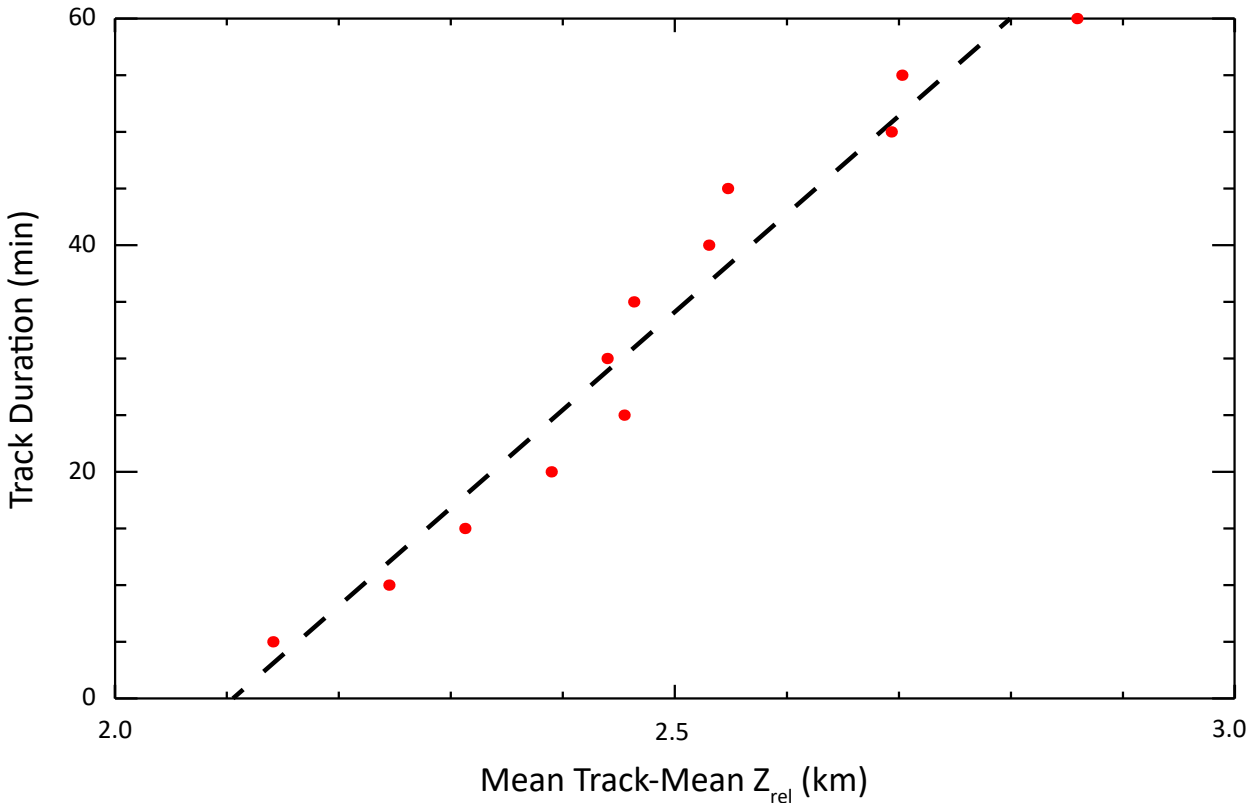

Figure 4.11: Mean of the track-mean Z_{rel}, binned by duration. Due to the small number of tracks with durations longer than 60 minutes, only shorter tracks are considered. The linear fit is shown in black with a slope of 86.5 minutes/km.

4.4 Overshoot Area

To characterize the overshoot area of a track, the mean region area is found for the duration of the track. A histogram of overshoot area is shown in Figure 4.12, along with the CDF and power-law fit. Due to the large number of bins with relatively few tracks at the tail end of the distribution, only bins with at least one track per day are considered. This corresponds to areas of up to ~800 km^2. The fit is applied by performing linear regression on the natural logarithm of the track count vs the natural logarithm of track-mean overshoot area. The resulting slope shows that: $n \propto a^{-1.67}$, where n is number of tracks and a is track-mean overshoot area in km^2.

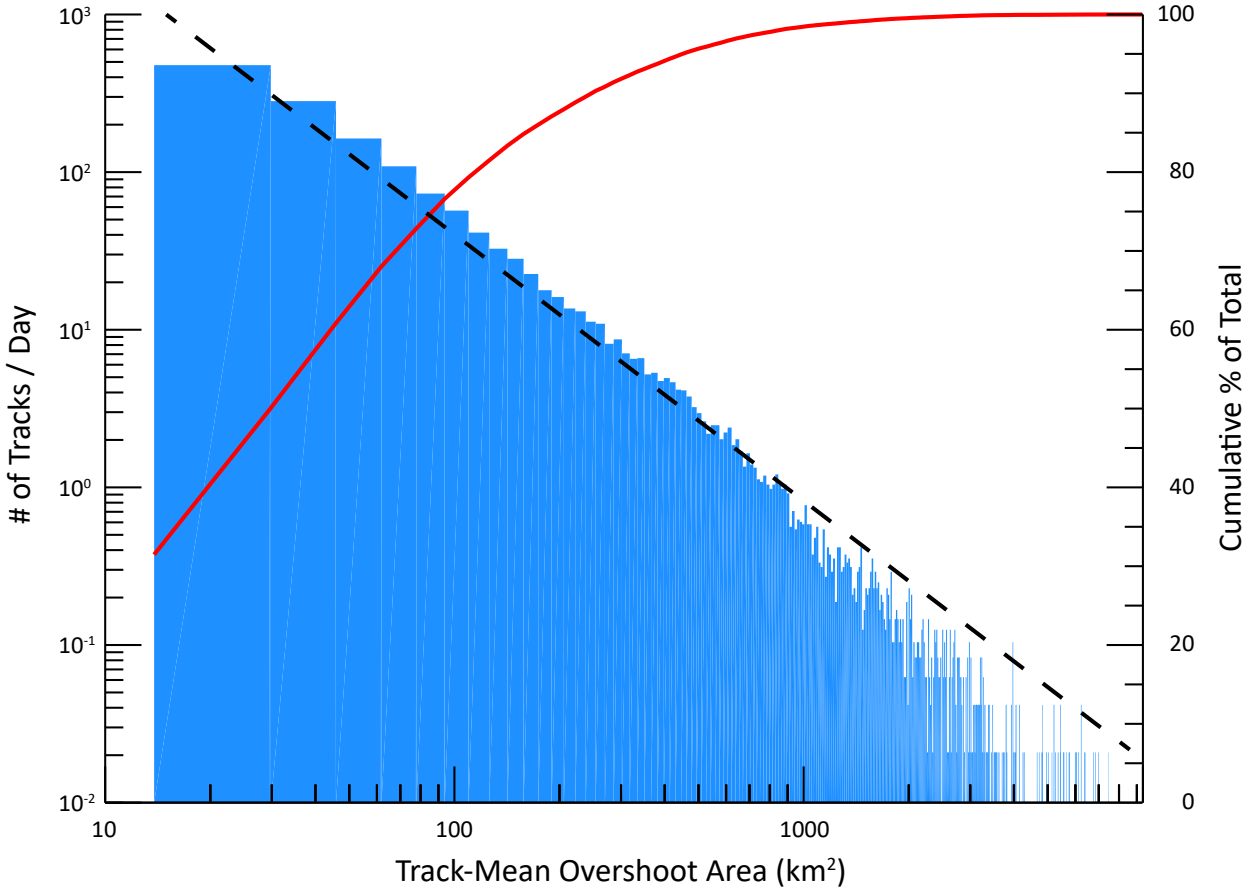

Figure 4.12: Pooled histogram of track-mean overshoot area for all sample periods. Bins are 16 km^2, which is approximately the average area of a four gridboxes within the analysis region. The cumulative distribution is shown in red. The dashed line represents a power-law fit with an exponent of about -1.67.

The geographic distribution of track-mean overshoot area is shown in Figure 4.13. There is a maximum over the central plains, corresponding to the region with the highest track count. This is also consistent with the observation that there are a large number of tracks from storm anvils in this region, as these can give rise to extreme overshoot-area values. There is a positive correlation between track-mean overshoot area and duration, shown in Figure 4.14. To generate this figure, track-mean overshoot-area values are first binned by track duration, and the mean of each bin is then found. A linear regression is applied to the plot, resulting in a fit with slope of 1.22 minutes/km^2. This implies that larger overshoots tend to last longer, which one might reasonably expect.

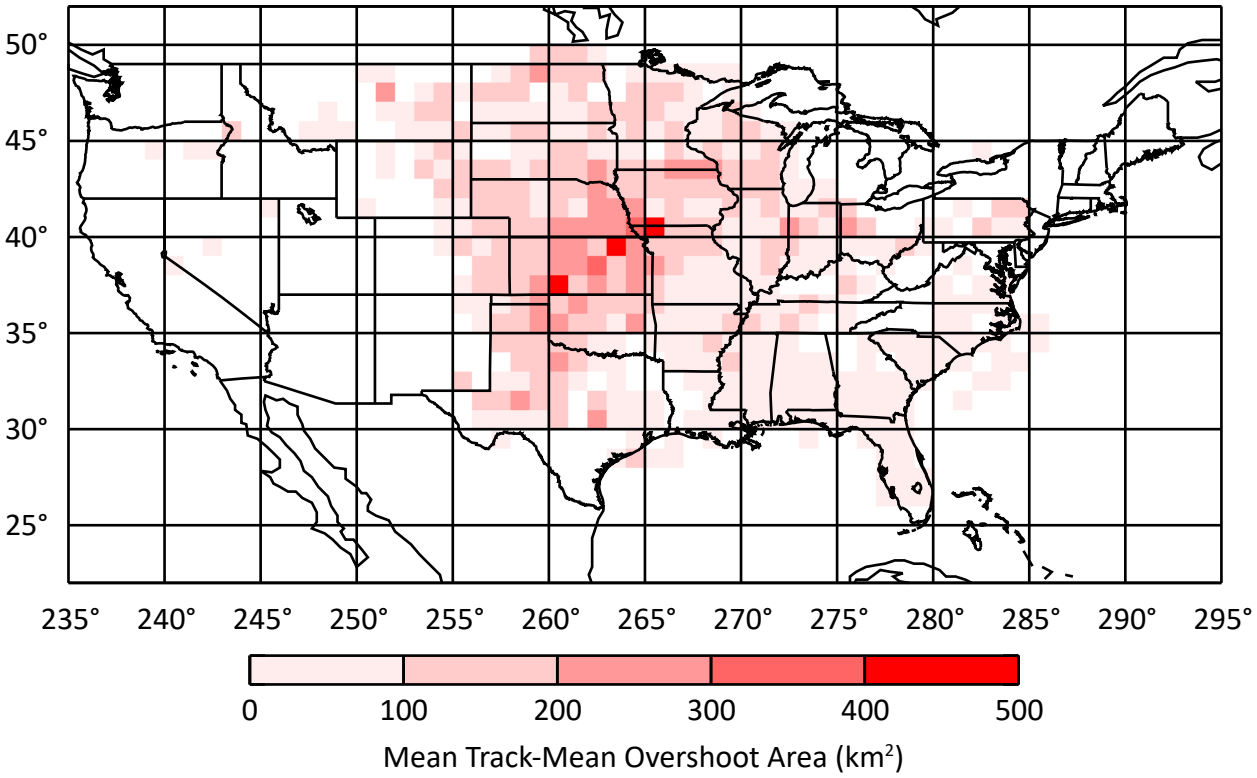

Figure 4.13: Geographic distribution of track-mean overshoot area. Mean values are shown for each 1° by 1° bin. Only bins with at least one track per day are shown.

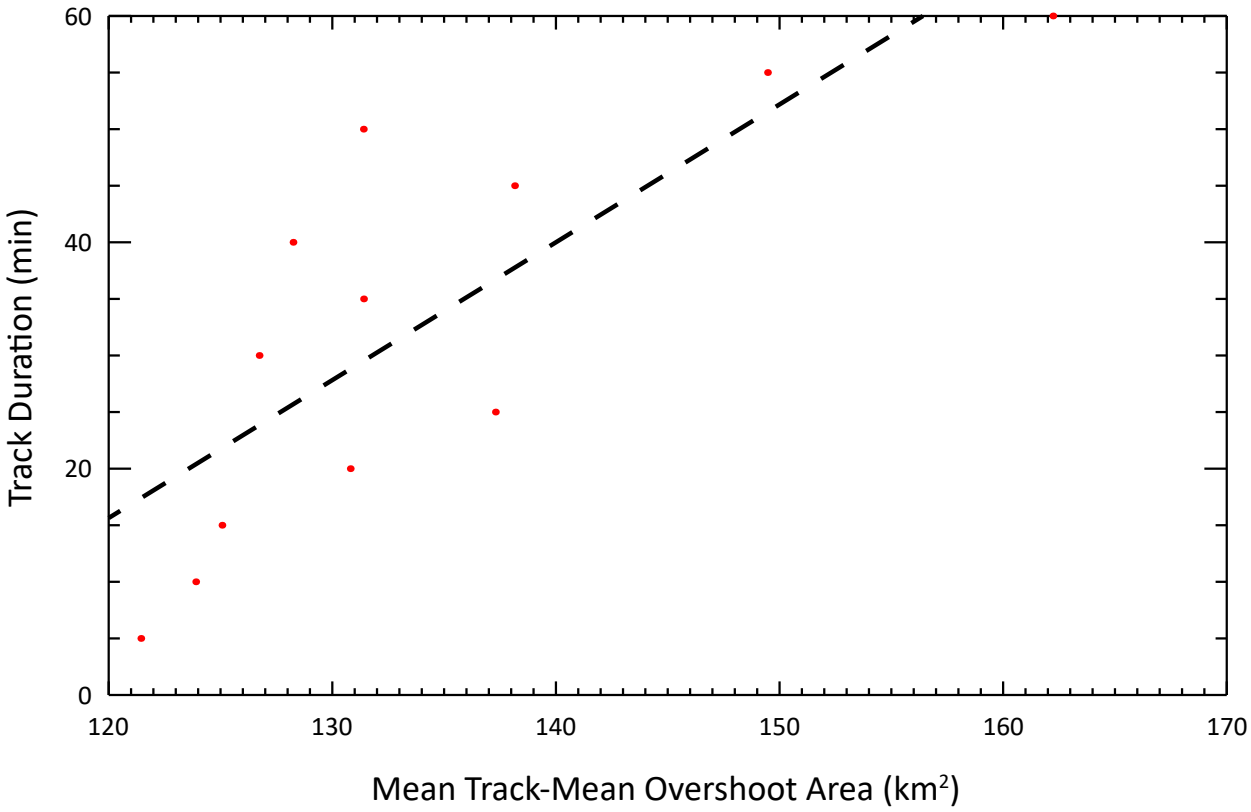

Figure 4.14: Mean of the track-mean overshoot area, binned by duration. Due to the small number of tracks with durations longer than 60 minutes, only shorter tracks are considered. The linear fit is shown in black with a slope of 1.22 min/km^2.

4.5 Column-Maximum Reflectivity

To characterize the updraft intensity for a track, the greatest column-maximum reflectivity values within each region are found at each timestep. These values are then averaged across the duration of the track. The histogram and CDF of these values are shown in Figure 4.15. There is a minimum threshold of 30 dBZ on the column-maximum reflectivity applied during tracking, so it is impossible for a track to have a lesser value. Approximately 95% of all tracks have a column-maximum reflectivity value below 60 dBZ, and the track count drops off rapidly at higher reflectivities. There is a distinct peak in the histogram at the 50-55 dBZ range. If we assume that greater reflectivity values indicate more intense updrafts and are therefore more likely to produce overshoots, and then consider that reflectivity values greater than 60 dBZ are somewhat rare, then we might expect the histogram to take this form. In other words, there is a 'sweet spot' in the reflectivity spectrum where the probability of overshooting and the frequency of occurrence combine to generate the greatest number of overshoots.

The geographic distribution of track-mean column-maximum reflectivity is shown in Figure 4.16. The values are rather homogeneous across the domain, dropping off slightly in the northwest over Montana, Wyoming, and the Dakotas. The relationship between column-maximum reflectivity and duration is shown in Figure 4.17. To generate this figure, track-mean column-maximum reflectivity values are first binned by track duration, and the mean of each bin is then found. An exponential fit is applied by performing linear regression on the natural logarithm of track duration vs track-mean column-maximum reflectivity. The resulting slope shows that $t \propto e^{a*cmax}$, where t is track duration, $cmax$ is the track-mean column-maximum reflectivity, and a is a constant with value 0.566. As column-maximum reflectivity is often used as a proxy for updraft strength, it is perhaps unsurprising that it is strongly related to overshoot duration.

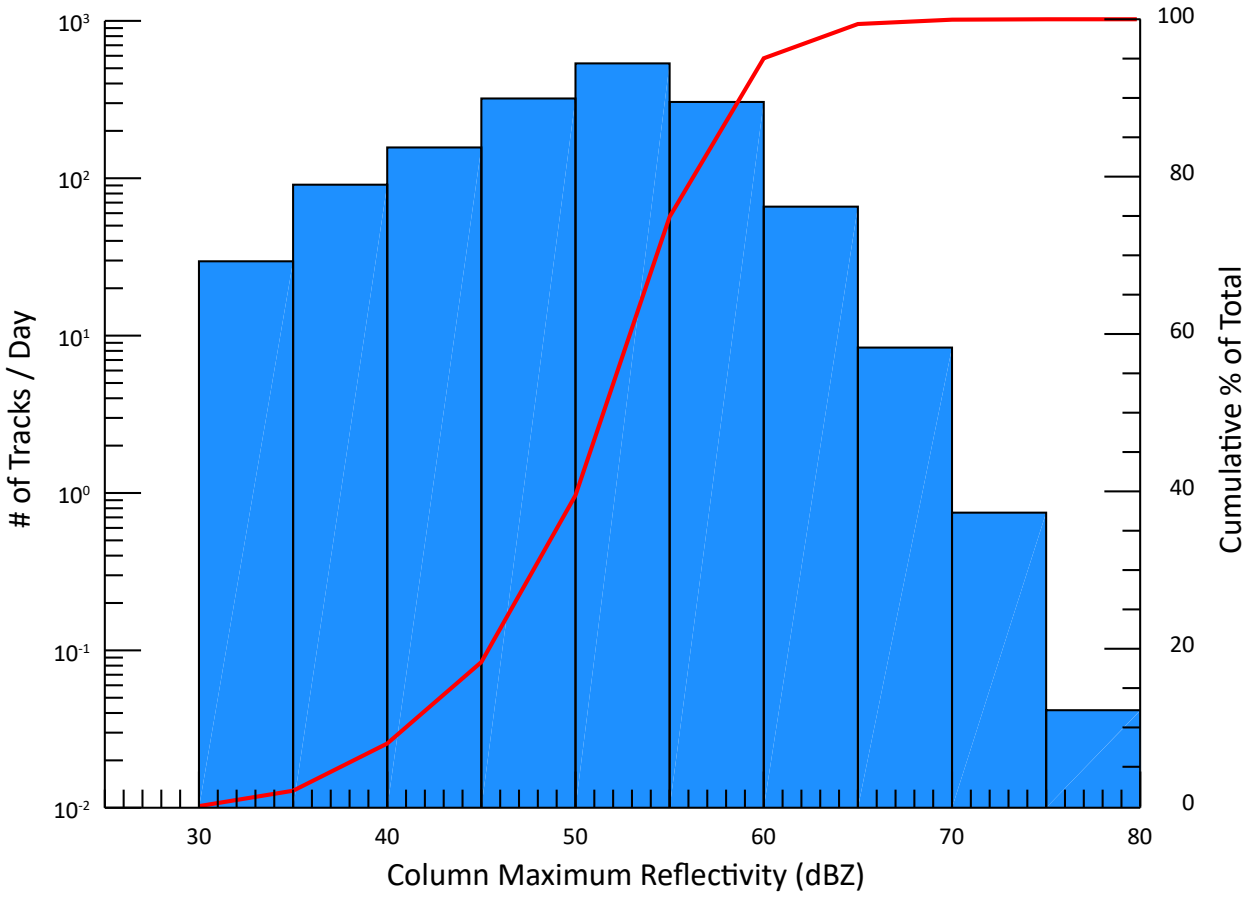

Figure 4.15: Pooled histogram of track column-maximum reflectivity for all sample periods. Bins are 5 dBZ wide. The cumulative distribution is shown in red.

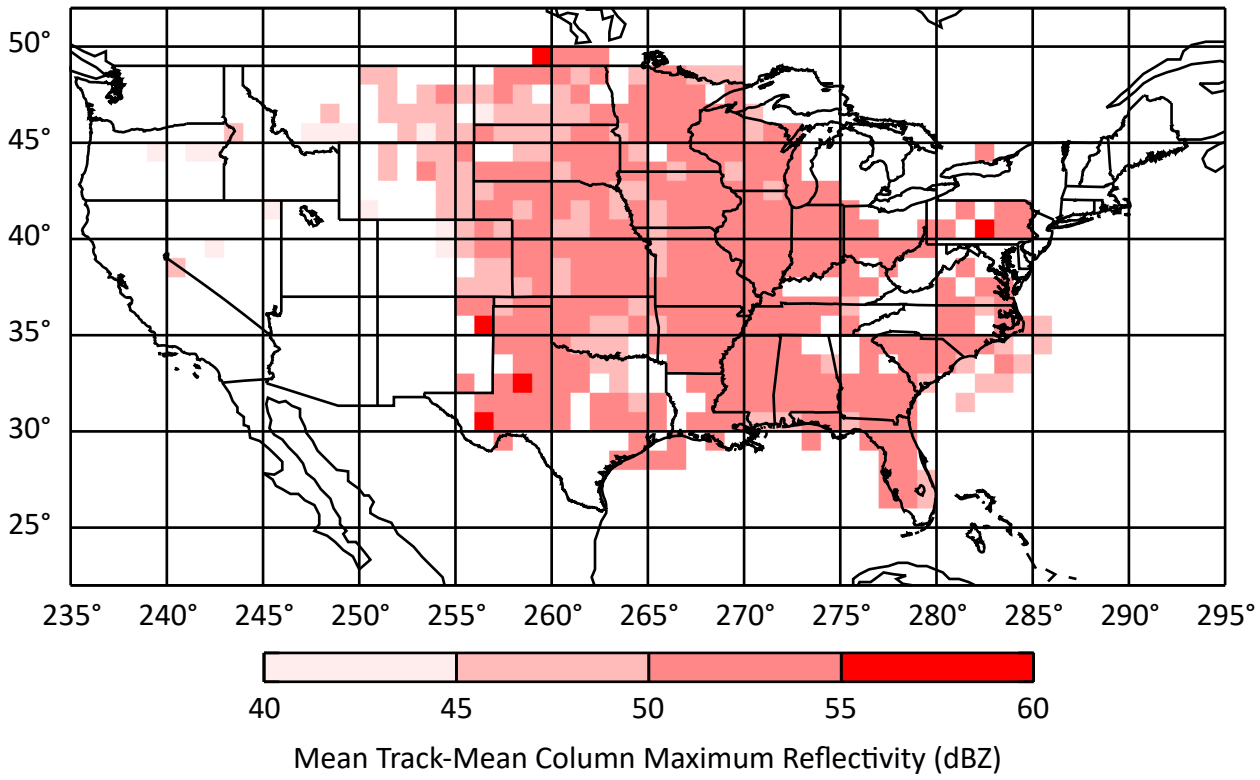

Figure 4.16: Geographic distribution of track-mean column-maximum reflectivity. Mean values are shown for each 1° by 1° bin. Only bins with at least one track per day are shown.

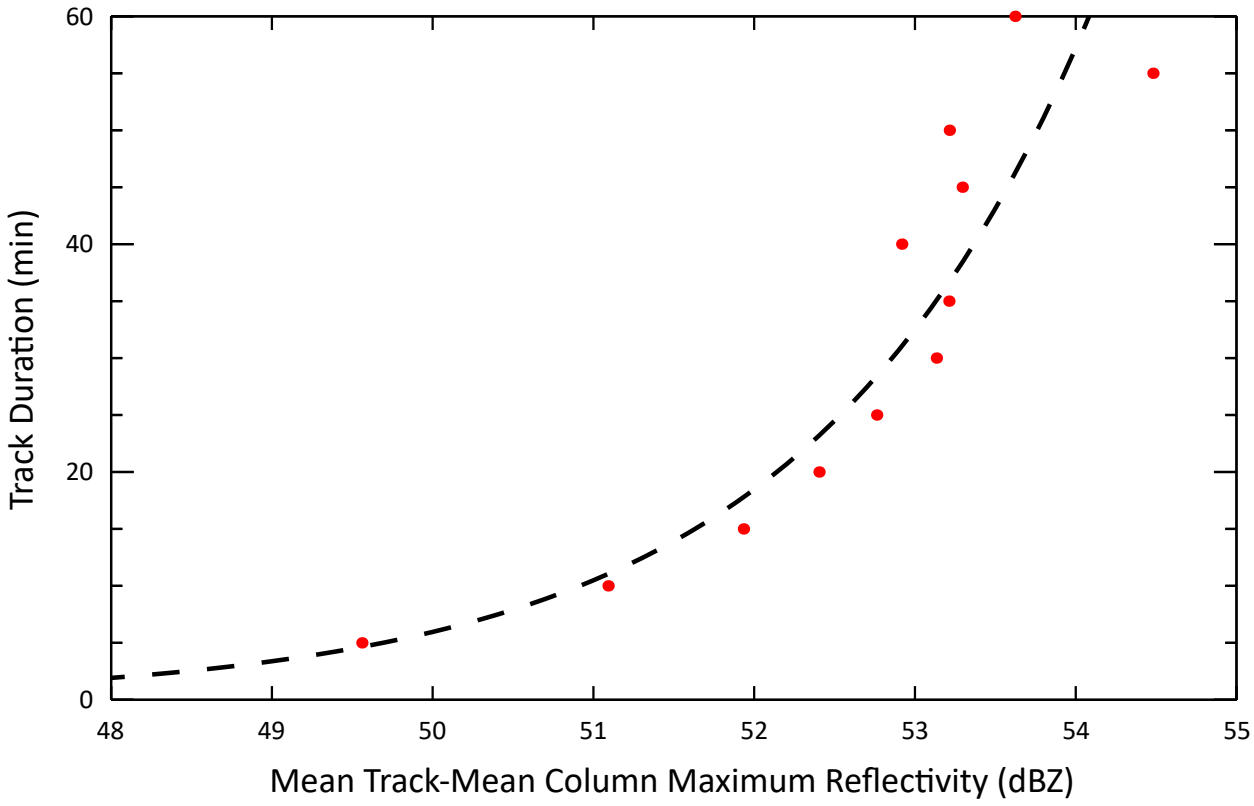

Figure 4.17: Mean of the track-mean column-maximum reflectivity, binned by duration. Due to the small number of tracks with durations longer than 60 minutes, only shorter tracks are considered. The exponential fit is shown in black.

4.6 Diurnal Cycle

The diurnal patterns in track initiation, duration, Z_{rel}, area, and column-maximum reflectivity are shown in Figure 4.18. Track start times are converted from UTC to local time (LT) based on the track longitude. Maximum track initiation occurs at 16 LT, and falls off to a minimum at 9 LT. This aligns reasonably well with the cycle in column-maximum reflectivity. The cycle in average duration peaks a few hours earlier, at 13 LT, while Z_{rel} and area peak later, at 19 and 21 LT respectively. Also shown are the first two harmonics of the Fourier transform. The amplitudes of these cycles are shown in Table 4.2. Track count and overshoot area show the greatest fluctuations throughout the day, while track-mean column-maximum reflectivity varies by only 5%. Considering the relationships between track duration and other track characteristics found above, it is surprising to find that their diurnal cycles are slightly out of phase. While it is not clear why this should be the case, we present a few possible explanations.

First, we must consider the diurnal heating cycle. This cycle peaks some time in the late afternoon/early evening, and we would expect this to coincide with maximum convective forcing, and consequently peak overshoot initiation and column-maximum reflectivity. However, overshoots that initiate before this peak in convective forcing will be more likely to continue to overshoot than those that initiate at or after the peak. This could explain why the peak in mean track duration is earlier than that of track count or mean column-maximum reflectivity. The next factor to consider is the potential discrepancy between the ERA5 tropopause and the actual, convectively-influenced tropopause. As discussed in the methods section, ERA5 is a hydrostatic model and does not resolve convection. Convective activity may raise the tropopause height locally, and if this is not properly represented in the ERA5 model this may result in large sections of anvil registering as overshooting. Naturally, we would expect this effect to be most prominent after convection has been ongoing for some time, and any underestimation in the ERA5 tropopause would result in larger overshoot areas and higher Z_{rel} values. This could explain why the cycles in mean Z_{rel} and mean overshoot area both peak later in the evening.

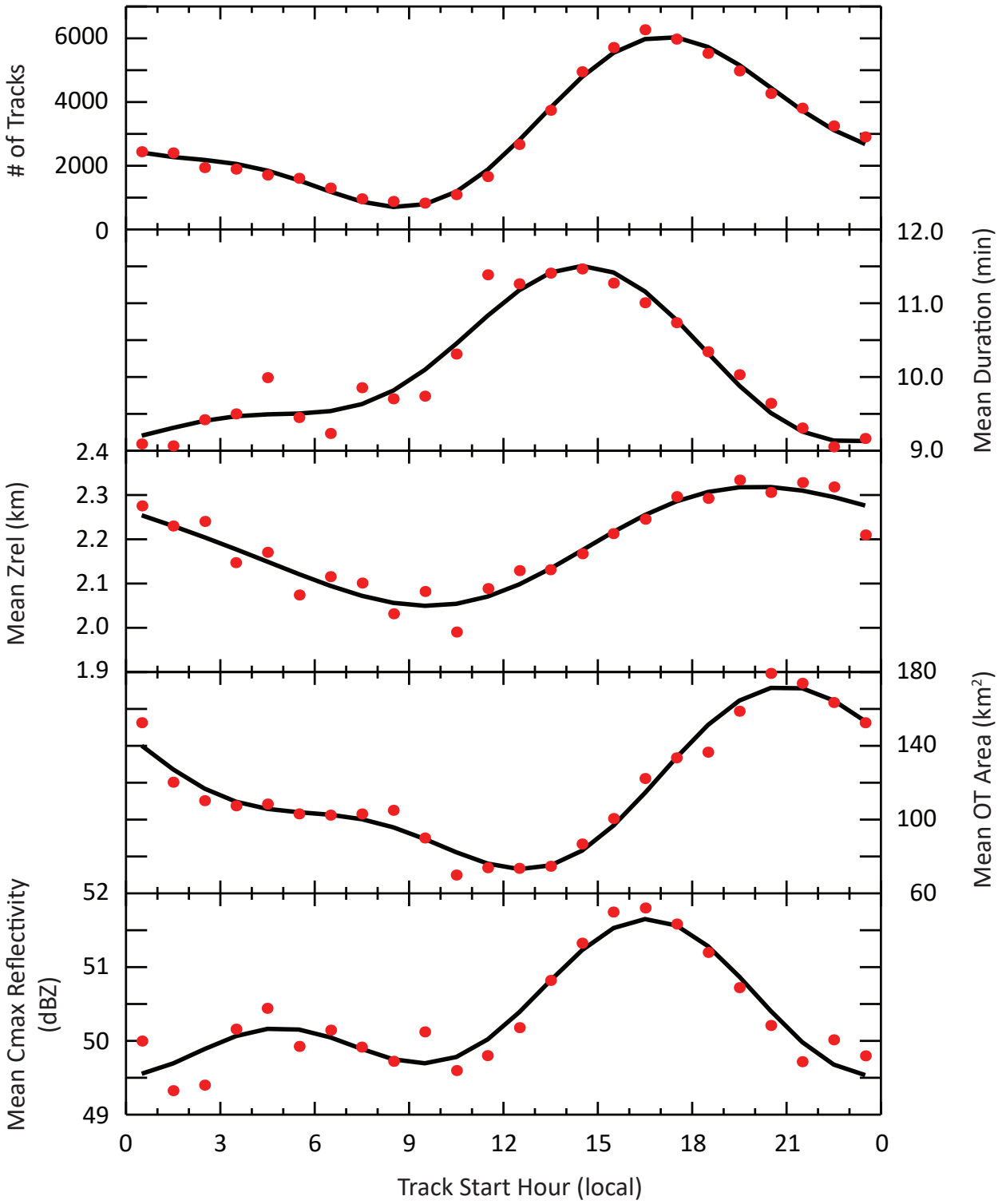

Figure 4.18: Descending: the number of tracks, mean track duration, mean tropopause-relative altitude, mean OT area, and mean column-maximum reflectivity by local start hour. The first two harmonics of the Fourier transform are shown in black.

	Diurnal Amplitude
Count	7.57
Duration	1.28
Mean Z_{rel}	1.15
Mean Area	2.57
Mean Cmax	1.05

Table 4.2: Amplitude of the diurnal cycle for various track characteristics (maximum value / minimum value).

5. CONCLUSIONS

This study aims to characterize the lifetimes of overshooting convective events. Data from the NEXRAD radar network is composited onto a three-dimensional grid to form GridRad analyses. Compositing is performed at 5-minute intervals for the 13th-17th of May, June, July, and August of 2017-2019. Overshooting regions are then identified by comparing the 10 dBZ echo-top heights with tropopause values derived from ERA5 reanalyses. A set of thresholds are applied to reduce noise and filter out unrealistic echo. The resulting region analyses match up well with the overshoot climatology presented in cooney, with a similar number of regions per analysis, diurnal cycle, and geographic distribution. Nearby regions in sequences of 5-minute analyses are linked to form tracks. To avoid edge effects, a 4-day sample window is selected from within each 5-day analysis period.

The final sample of 72,779 overshoot tracks provides information on the durations of overshoots and their distribution. Half of these tracks consist of a single, unlinked timestep, but 25% are observed to last longer than the Brunt-Väisälä period in the UTLS (around 10 minutes), and the longest observed track has a duration of over 2 hours. A histogram of track duration shows that track count falls off approximately exponentially with an e-folding timescale of about 8 minutes. The relationships between duration and various track characteristics are also examined. Longer storms are found to penetrate further into the stratosphere, and to have larger overshoot areas. An exponential relationship is observed between column-maximum reflectivity and track duration, implying that a strong updraft is critical to the formation of a long-lived overshooting top.

Geographic variations in the number of tracks and their characteristics are also considered. From the results, two main regions of interest are identified: the central plains, namely Kansas and Nebraska, and the southeast, namely Alabama and Georgia. The central plains feature a maximum in track initiation, tropopause-relative altitude, and overshoot area, yet the track durations in this region are shorter on average. Further investigation reveals that this is most likely the result of the large number of single-timestep tracks that form from storm anvils over the central plains, though

it is unclear why this should be the case. In contrast, the southeast region has far fewer of these anvil tracks, but is still a secondary maximum for track initiation. As a result, the mean durations of tracks in this region are longer.

There are clear diurnal cycles in track count, duration, mean Z_{rel}, mean overshoot area, and mean column-maximum reflectivity. Track count and area have the strongest diurnal signals, while mean column-maximum reflectivity varies only slightly throughout the day. These cycles are out of phase, with mean track duration peaking around 15 LT, followed by track count and mean column-maximum reflectivity at 17 LT, and finally mean Z_{rel} and mean overshoot area near 21 LT.

The primary motivation for this study is to increase our understanding of the role overshooting convection plays in transporting water vapor and other chemical species from the troposphere into the stratosphere. With this in mind, the largest and longest lasting overshoots are of the greatest importance. Overshoot location is also quite relevant when considering potential stratospheric impacts. Material that is injected over the central plains will be contained within the North American Monsoon Anticyclone (NAMA) to a greater extent than material injected over the southeast US. This increased residence time will lead to higher concentrations and a larger impact on the chemistry of the stratosphere.

Overall, the accuracy of these results is impacted by a lack of radar sweeps at higher elevation angles, leading to overestimation in the number of short-lived overshoots. Also, large sections of the anvil frequently register as overshooting, even with the minimum Z_{rel} requirement of 1 km. This results in many large overshooting regions, affecting the overshoot area statistics. However, many of the longest-lived tracks appear realistic under manual inspection, and this study provides a good survey of the typical lifetimes of overshoots and their relationships to other track parameters. Future work could include algorithm improvements to better identify track splitting/merging, and utilizing additional overshoot-detection techniques such as satellite imagery to more accurately identify overshooting regions.

REFERENCES

[1] J. W. Cooney, K. P. Bowman, C. R. Homeyer, and T. M. Fenske, "Ten year analysis of tropopause-overshooting convection using GridRad data," *Journal of Geophysical Research: Atmospheres*, vol. 123, no. 1, pp. 329–343, 2018.

[2] A. W. Brewer, "Evidence for a world circulation provided by the measurements of helium and water vapour distribution in the stratosphere," *Quarterly Journal of the Royal Meteorological Society*, vol. 75, no. 326, 1949.

[3] G. M. B. Dobson, "Origin and distribution of the polyatomic molecules in the atmosphere," *Proceedings of the Royal Society at London*, vol. 236A, 1956.

[4] T. Flury, D. L. Wu, and W. G. Read, "Variability in the speed of the Brewer–Dobson circulation as observed by Aura/MLS," *Atmospheric Chemistry and Physics*, vol. 13, no. 9, 2013.

[5] K. Minschwaner and J. H. Jiang, "The upward branch of the Brewer-Dobson circulation quantified by tropical stratospheric water vapor and carbon monoxide measurements from the Aura Microwave Limb Sounder," *JGR: Atmospheres*, vol. 121, no. 6, 2016.

[6] D. L. Solomon, K. P. Bowman, and C. R. Homeyer, "Tropopause-penetrating convection from three-dimensional gridded NEXRAD data," *Journal of Applied Meteorology and Climatology*, vol. 55, no. 2, pp. 465–478, 2016.

[7] C. R. Homeyer and K. P. Bowman, "A 22-year evaluation of convection reaching the stratosphere over the united states," *JGR: Atmospheres*, vol. 126, no. 13, 2021.

[8] J. Aschmann, B. Sinnhuber, M. Chipperfield, and R. Hossaini, "Impact of deep convection and dehydration on bromine loading in the upper troposphere and lower stratosphere," *Atmospheric Chemistry and Physics*, vol. 11, no. 6, pp. 2671–2687, 2011.

[9] Q. Tang, M. J. Prather, and J. Hsu, "Stratosphere-troposphere exchange ozone flux related to deep convection," *Geophysical Research Letters*, vol. 38, no. 3, 2011.

[10] M. R. Sargent, J. B. Smith, D. S. Sayres, and J. G. Anderson, "The roles of deep convection and extratropical mixing in the tropical tropopause layer: An in situ measurement perspective," *Journal of Geophysical Research: Atmospheres*, vol. 119, no. 21, 2014.

[11] W. J. Randel, K. Zhang, and R. Fu, "What controls stratospheric water vapor in the NH summer monsoon regions?," *Journal of Geophysical Research: Atmospheres*, vol. 120, no. 15, pp. 7988–8001, 2015.

[12] W. Yu, A. E. Dessler, M. Park, and E. J. Jensen, "Influence of convection on stratospheric water vapor in the north american monsoon region," *Atmospheric Chemistry and Physics*, vol. 20, no. 20, pp. 12153–12161, 2020.

[13] L. Zou, L. Hoffmann, S. Griessbach, R. Spang, and L. Wang, "Empirical evidence for deep convection being a major source of stratospheric ice clouds over North America," *Atmospheric Chemistry and Physics*, vol. 21, no. 13, pp. 10457–10475, 2021.

[14] K. M. Bedka, "Overshooting cloud top detections using MSG SEVIRI infrared brightness temperatures and their relationship to severe weather over Europe," *Atmospheric Research*, vol. 99, no. 2, pp. 175–189, 2011.

[15] P. Mikuš and N. Strelec Mahović, "Satellite-based overshooting top detection methods and an analysis of correlated weather conditions," *Atmospheric Research*, vol. 123, pp. 268–280, 2013.

[16] K. M. Bedka, J. T. Allen, H. J. Punge, M. Kunz, and D. Simanovic, "A long-term overshooting convective cloud-top detection database over australia derived from MTSAT Japanese Advanced Meteorological Imager Observations," *Journal of Applied Meteorology and Climatology*, vol. 57, no. 4, pp. 937–951, 2018.

[17] K. Bedka, E. M. Murillo, C. R. Homeyer, B. Scarino, and H. Mersiovsky, "The above-anvil cirrus plume: An important severe weather indicator in visible and infrared satellite imagery," *Weather and Forecasting*, vol. 33, no. 5, 2018.

[18] T. D. Crum and R. L. Albery, "The WSR-88D and the WSR-88D operational support facility," *Bulletin of the American Meteorological Society*, vol. 74, no. 9, pp. 1669–1687, 1993.

[19] H. Hersbach, B. Bell, P. Berrisford, S. Hirahara, A. Horányi, J. Muñoz-Sabater, J. Nicolas, C. Peubey, R. Radu, D. Schepers, A. Simmons, C. Soci, S. Abdalla, X. Abellan, G. Balsamo, P. Bechtold, G. Biavati, J. Bidlot, M. Bonavita, G. De Chiara, P. Dahlgren, D. Dee, M. Diamantakis, R. Dragani, J. Flemming, R. Forbes, M. Fuentes, A. Geer, L. Haimberger, S. Healy, R. J. Hogan, E. Hólm, M. Janisková, S. Keeley, P. Laloyaux, P. Lopez, C. Lupu, G. Radnoti, P. de Rosnay, I. Rozum, F. Vamborg, S. Villaume, and J.-N. Thépaut, "The ERA5 global reanalysis," *Quarterly Journal of the Royal Meteorological Society*, vol. 146, no. 730, 2020.

[20] J. Zhang, K. Howard, and J. J. Gourley, "Constructing three-dimensional multiple-radar reflectivity mosaics: Examples of convective storms and stratiform rain echoes," *Journal of Atmospheric and Oceanic Technology*, vol. 22, no. 1, pp. 30–42, 2005.

[21] J. Zhang, K. Howard, C. Langston, S. Vasiloff, B. Kaney, A. Arthur, S. Van Cooten, K. Kelleher, D. Kitzmiller, F. Ding, D.-J. Seo, E. Wells, and C. Dempsey, "National mosaic and multi-sensor QPE (NMQ) system: Description, results, and future plans," *Bulletin of the American Meteorological Society*, vol. 92, no. 10, pp. 1321–1338, 2011.

[22] A. Jurczyk, J. Szturc, and K. Ośródka, "Quality-based compositing of weather radar derived precipitation," *Meteorological Applications*, vol. 27, no. 1, 2019.

[23] C. R. Homeyer and K. P. Bowman, "Algorithm description document for version 3.1 of the three-dimensional Gridded NEXRAD WSR-88D Radar (GridRad) dataset," 2017.

[24] T. Reichler, M. Dameris, and R. Sausen, "Determining the tropopause height from gridded data," *Geophysical Research Letters*, vol. 30, no. 20, 2003.

[25] S. Tegtmeier, J. Anstey, S. Davis, R. Dragani, Y. Harada, I. Ivanciu, R. P. Kedzierski, K. Krüger, B. Legras, C. Long, J. S. Wang, K. Wargan, and J. S. Wright, "Temperature and tropopause characteristics from reanalyses data in the tropical tropopause layer," *Atmospheric Chemistry and Physics*, vol. 20, no. 2, 2020.

APPENDIX A

SENSITIVITY ANALYSIS

It is necessary to consider the sensitivity of these results to chosen parameters. The thresholds chosen for minimum Z_{rel} and minimum region size will determine how many overshoot regions are identified at each time step, while the selected search radius will impact track formation. In order to investigate to what extent these choices impact the results of this study, tracking is carried out with seventeen different combinations of parameters (see Table A.1). Note that an older echo-top algorithm is used for this comparison, so there is no 30 dBZ column-maximum reflectivity requirement. For the figures in this section, the analysis titles indicate what parameters are used, with 'minpix_4' corresponding to a minimum region-size requirement of four gridboxes, and 'minz_1' corresponding to a minimum tropopause-relative altitude of 1km. The analysis labelled 'raw' is run with no thresholds whatsoever. For the first set of analyses, the search radius is kept the same at 7 km while the minimum Z_{rel}, and minimum region-size are allowed to vary. Figures A.1 and A.2 show the histograms of duration and area respectively for a range of minimum region sizes (0, 4, or 9 gridboxes) and minimum tropopause-relative altitudes (0, 1, or 2 km). The impact of these thresholds on the distribution of durations appears to be minimal, having nearly identical normalized histograms with mean values varying from 553 s to 590 s with a standard deviation of 12.3 s. The area histograms have similar slopes, and naturally are most affected by the minimum area thresholds. These thresholds act to shift the histogram toward higher area values, but otherwise preserve the shape of the histogram. The initial upward slope of each histogram is an artifact of the bin locations, which correspond roughly to integer numbers of gridboxes. The stricter thresholds reduce the total number of tracks significantly, as shown in A.2. In an attempt to filter out the least impactful overshooting events while retaining a substantial number of tracks for analysis, moderate thresholds of 1 km minimum Z_{rel} and a minimum region size of 4 gridboxes are selected (analysis name 'minz1_minpix4').

		Minimum Z_{rel}		
		0	1	2
Minimum Region Size (Gridboxes)	1	7 km	7 km	7 km
	4	7 km	2-10 km	7 km
	9	7 km	7 km	-

Table A.1: Search Radii used for various combinations of the minimum region-size and minimum Z_{rel} requirements.

Next, tracking is run with these chosen thresholds for a range of search radii, from 2-10 km. As the interval between analyses is 5 minutes, the search radius can be interpreted as a maximum storm speed. The maximum speeds tested therefore range from 24-120 km/h. The resulting histograms of duration and area are shown in figures A.3 and A.4. Clearly, this parameter has much more of an impact on the statistics of the resulting tracks. Area is nearly unaffected, while the slopes of the duration histograms vary greatly. Mean duration values range from 349 s for a search radius of 5 km to 738 s for a search radius of 10 km with a standard deviation of 126 s. The distributions remain approximately exponential, but are shifted toward shorter durations for shorter search radii, and longer durations for longer search radii. Therefore, it is important to justify our choice of search radius through physical reasoning as much as possible. Search radii of 4 km or less correspond to a single gridbox or less, and are therefore quite limiting. It is necessary to allow for some uncertainty in the updraft location as indicated by radar echo, as well as for motion of the storm itself. On the upper end, a search radius of 8 km corresponds to a storm speed of 96 km/h, which is faster than we expect storms to be moving. However, the location of the overshooting region has greater variability than that of the storm itself, as it is defined to be the gridbox with the greatest Z_{rel} which may change without any storm motion whatsoever. Still, the choice is made to not consider search radii of 8 km or more, both for the physical reasoning outlined above as well as to minimize the incorrect linking of discrete, yet nearby OTs. A 7 km search radius is selected, as it provides the largest sample of tracks for analysis while minimizing improbable matches.

Analysis Name	Number of Tracks	Mean Track Duration	Mean Track Area
minpix4	207620	589.778	157.562
minpix9	132359	581.673	242.780
minz1	208462	567.512	52.7195
minz1_minpix4_sr10	69824	737.673	114.510
minz1_minpix4_sr2	147535	349.103	135.756
minz1_minpix4_sr3	129941	396.376	135.313
minz1_minpix4_sr4	120321	428.070	135.646
minz1_minpix4_sr5	103778	496.316	132.661
minz1_minpix4_sr6	93227	552.490	129.545
minz1_minpix4_sr7	87326	589.862	128.405
minz1_minpix4_sr7_NOAN	92350	585.083	114.958
minz1_minpix4_sr8	78873	653.041	122.858
minz1_minpix4_sr9	74855	688.114	119.528
minz1_minpix9_sr7	57235	576.607	191.590
minz2	76763	553.016	46.6099
minz2_minpix4_sr7	35636	573.827	102.345
raw	562124	583.314	56.9643

Table A.2: Statistics for the different analyses run during sensitivity testing.

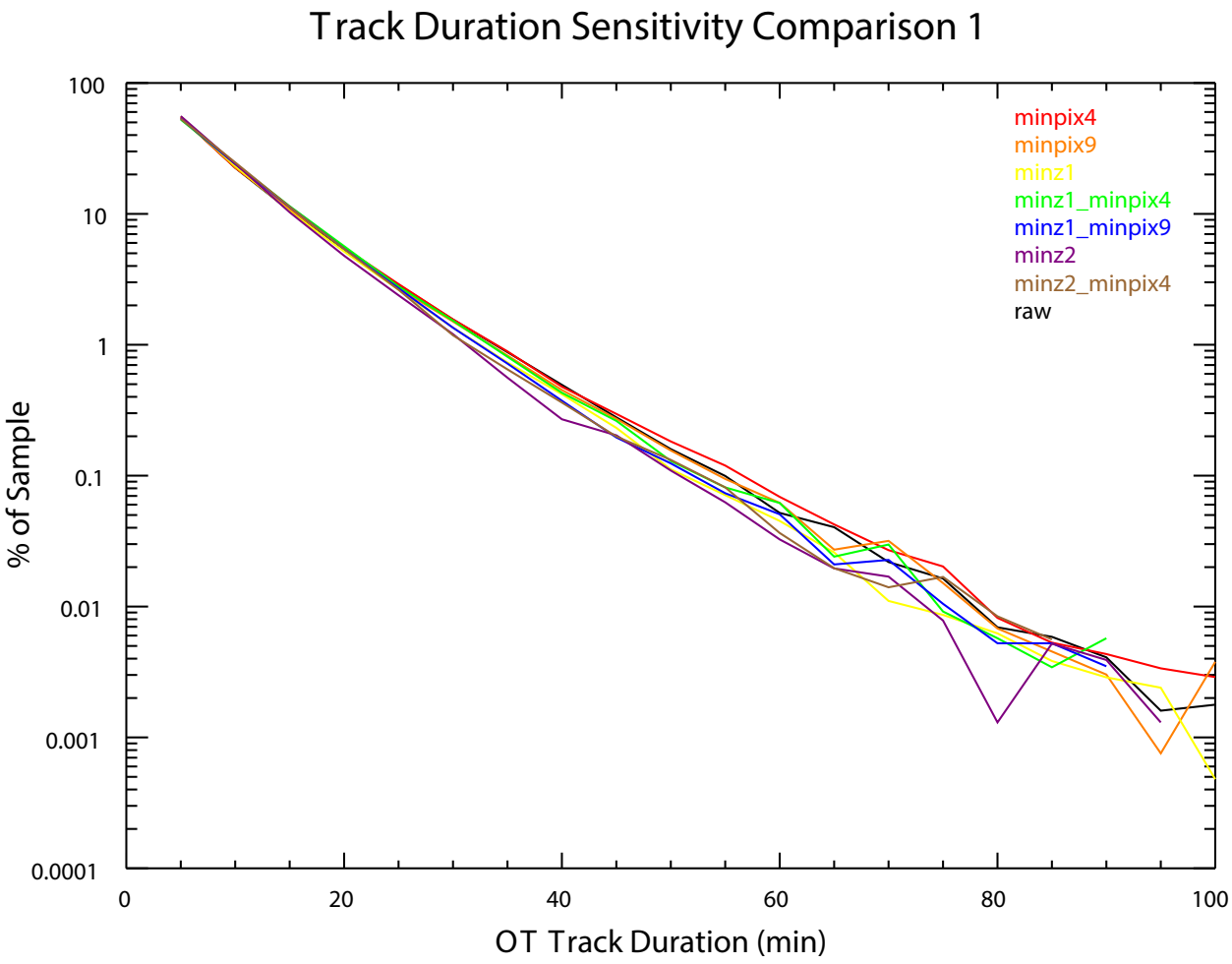

Figure A.1: Histograms of track duration for several combinations of tracking parameters. All analyses in this comparison have a maximum search radius of 7 km.

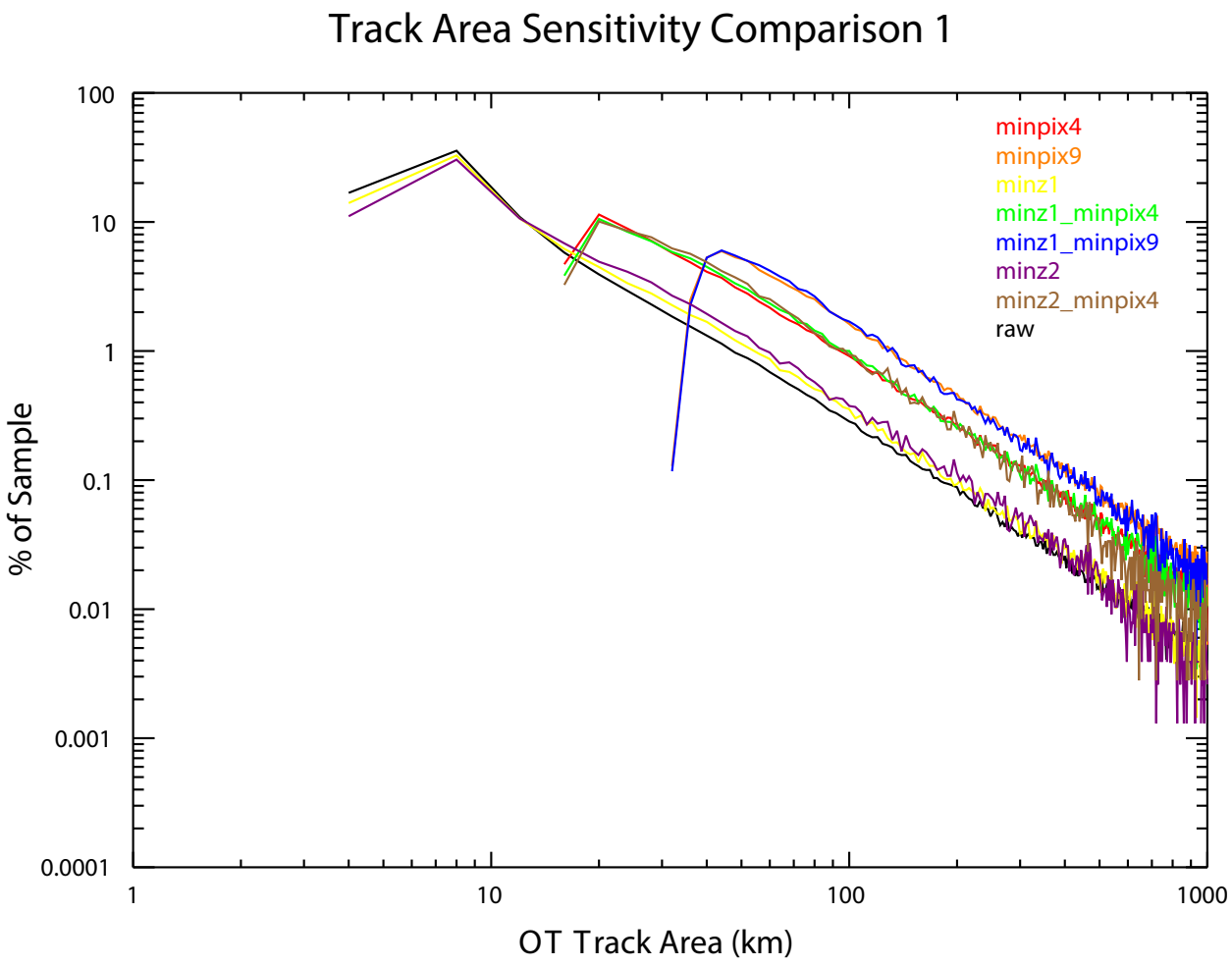

Figure A.2: Histograms of mean overshoot area for several combinations of tracking parameters. All analyses in this comparison have a maximum search radius of 7 km.

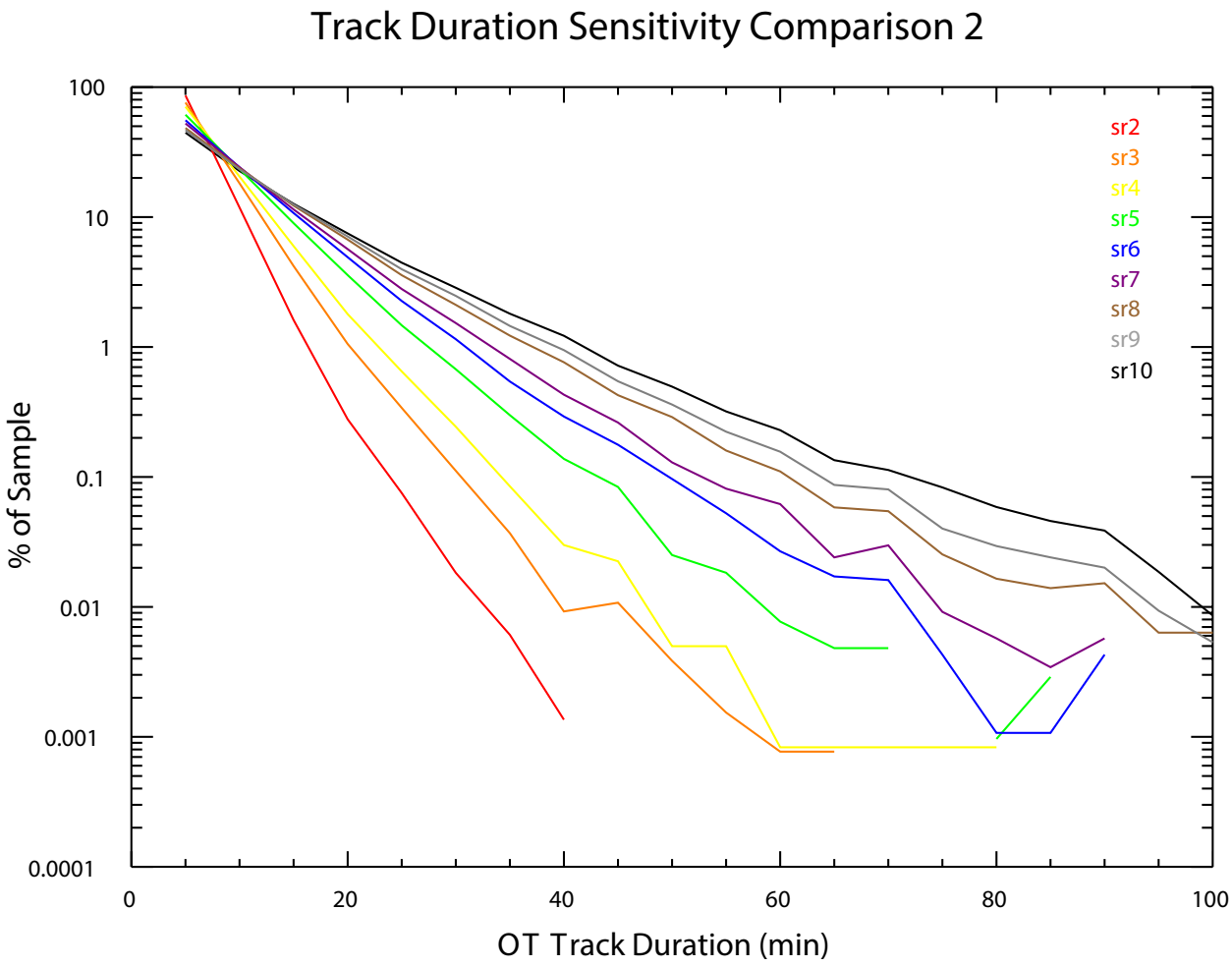

Figure A.3: Histograms of track duration for several different search radii. All analyses in this comparison have a minimum Z_{rel} threshold of 1 km, and minimum region size of 4 gridboxes.

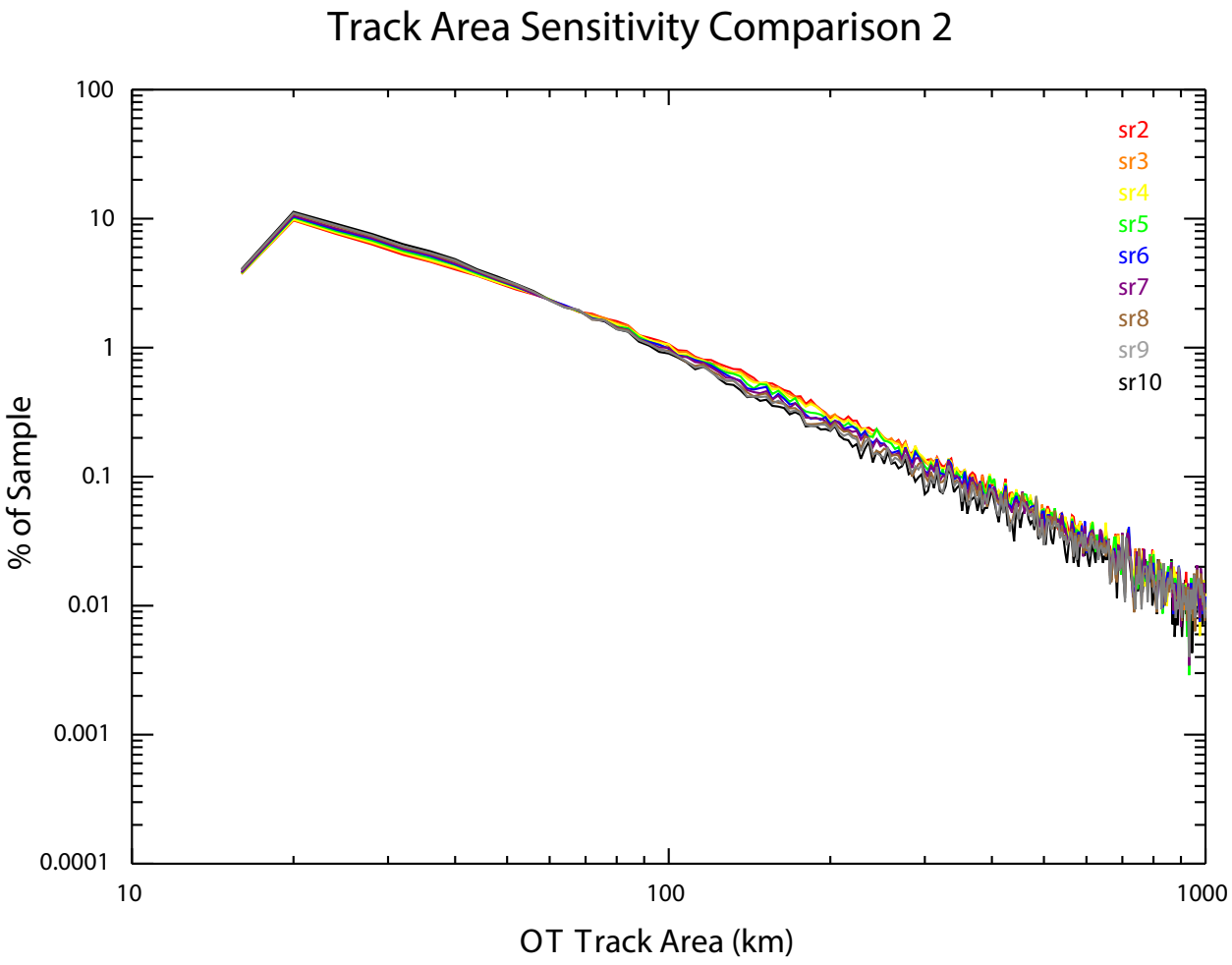

Figure A.4: Histograms of mean overshoot area for several different search radii. All analyses in this comparison have a minimum Z_{rel} threshold of 1 km, and minimum region size of 4 gridboxes.